THE EVOLUTION AND DYNAMICS OF SPARK GENERATED SHOCK WAVES AND THEIR FOCUSING BY ELLIPSOIDAL REFLECTORS IN LITHOTRIPSY

BY

MOHAMED E. NASR

A DISSERTATION PRESENTED TO THE GRADUATE SCHOOL
OF THE UNIVERSITY OF FLORIDA IN
PARTIAL FULFILLMENT OF THE REQUIREMENTS
FOR THE DEGREE OF DOCTOR OF PHILOSOPHY

UNIVERSITY OF FLORIDA

1986

ACKNOWLEDGMENTS

This project is typical of inter-disciplinary endeavors involving the skill and talent of individuals from a wide range of backgrounds. I would like to take this opportunity to thank a few individuals in particular for the invaluable assistance they gave me.

I would like to express my sincere gratitude to Professor Ulrich H. Kurzweg, the chairman of my doctoral committee, for his teaching and assistance throughout my graduate studies at the University of Florida. He provided not only the opportunity but also the much needed encouragement and guidance as well as bringing about my financial support through the Egyptian Educational Bureau.

The author is in great debt to Professor Birdwell Finlayson, my committee cochairman not only for his help and encouragement but also for financially supporting this research project.

Dr. Harold Doddington's assistance with electrical circuits and instrumentation afforded me valuable experience.

I also wish to thank the other members of my Doctoral committee, Dr. Lawrence Malvern, Dr. Edward Walsh, Dr. A.

Varma, and Dr. Charles Taylor, for valued advice they were able to offer me during my graduate studies.

Finally, I would like to express my sincere appreciation to my wife Noha for her patience, understanding and encouragement without which it would have been almost impossible to finish this project. I wish to also extend my sincere appreciation to my parents for their help and encouragement.

TABLE OF CONTENTS

Page

ACKNOWLEDGMENTS ii

ABSTRACT vi

CHAPTER I INTRODUCTION 1

The Problem of Uninary Stones 1
Methods of Treatment 1
Previous Investigations on the Use of Spark Generated Shocks 5
Water Breakdown 6
Dissipation of Energy 8
Focusing of Shock Waves 9
Cavitation Phenomenon 10
ESW as a Fracture Mechanism 12

CHAPTER II EXPERIMENTAL APPARATUS AND PROCEDURES . . . 14

Listing of the Experiment Equipment 14
Features of Some Individual Components . . . 15
Practical Problems with Commercial Transducers 27
Peizoelectric Crystals 30
Design Characteristics of the Transducer . . 39
Experimental Procedures 41

CHAPTER III ANALYTICAL AND EXPERIMENTAL BACKGROUND . . 51

Underwater Shock Wave Generating Mechanisms 51
Shock Waves 53
Dissipative Mechanisms and the Width of the Shock Front 59
Cavitation Phenomenon 62
Collapse Times of Gas Bubbles 62
The Optimum Peak Pressure 63
Principles of Modelling of Urinary Test Concretions 63

Page

CHAPTER IV EXPERIMENTAL RESULTS 70

Analysis of the Characteristics of the ESWL . 74
Shock Generating Mechanisms 88
Analysis of Direct Shock Wave (DSW) 89
Characteristics of Focused Shock Wave 100
EHL Reflected Shock Wave Analysis 115
Cavitation Phenomenon at the First
Focus (F1) 122
Shock Test of Simulated Urinary Stones . . . 133

CHAPTER V SUMMARY AND CONCLUSIONS 143

LIST OF REFERENCES 157

BIOGRAPHICAL SKETCH 164

Abstract of Dissertation Presented to the Graduate School
of the University of Florida in Partial Fulfillment of the
Requirements for the Degree of Doctor of Philosophy

THE EVOLUTION AND DYNAMICS OF SPARK GENERATED SHOCK WAVES AND THEIR FOCUSING BY ELLIPSOIDAL REFLECTORS IN LITHOTRIPSY

By

Mohamed E. Nasr

December, 1986

Chairman: Dr. Ulrich H. Kurzweg
Cochairman: Dr. Birdwell Finlayson
Major Department: Engineering Sciences

This is an experimental investigation of the evolution, propagation, and focusing of shock waves generated by an electrical discharge at the first focus (F1) of a rotationally symmetric ellipsoidal reflector. The electric spark induces an initial spherical shock wave part of which propagates directly along the Z axis connecting the two foci of the reflector. This shock wave is referred to as the Direct Shock Wave (DSW). The remaining portion of the spherical shock impinges on the reflector boundary, and this generates a new shock wave which propagates toward the second focus (F2) of the ellipsoid. This focused shock wave is referred to as the Reflected Shock Wave (RSW).

The characteristics of the DSW as well as the RSW are examined in both the time domain and the space domain. The characteristics studied include pressure, propagation velocity, energy flux density, shock impulse, as well as the shock duration and rise time. In addition, we have examined the characteristics of Extracorporeal Shock Wave Lithotriptors (ESWL) and in particular the intensity and focusing quality of the RSW. Other characteristics examined include the input voltage, the carrier fluid (water) conditions, the electrode spark gap wear and the inflation of the para-ellipsoid balloons. Furthermore, a cavitation phenomena was found to follow both the DSW at F1 and the RSW at F2. These have been examined in terms of the dynamic impact pressure, the energy stored within the plasma of the bubble, the velocity of both expansion and contraction of the bubble, as well as the radius history of the cavitation.

The effect of both mechanisms, the RSW and the cavitation bubble at F2 on the urinary stones is examined. Urinary calculi have been modelled in terms of their compressive strength. These simulated urinary test concretions have been shock tested along the reflector Z axis and their fracture patterns have been analyzed.

The results of this experimental investigation are expected to find application in improving the lithotripsy technique presently being used to fracture urinary calculi and may furnish the basis for developing of improved theories for the fracture mechanism produced by focused shocks.

CHAPTER I

INTRODUCTION

The Problem of Urinary Stones

Urinary stones in the human bladder and kidney are a major medical problem throughout the world and also throughout the course of recorded and pre-recorded history. For example, an ancient cemetery dating from about 4800 B.C. in El-Amrah, upper Egypt, holds the grave of a 16-year-old youth who had a 6.6 cm bladder stone.

The exact reasons and manner of stone formation are not all well understood. The tendency to form stones varies between cultures and geographic areas.

Small stones, early in formation, may pass through the urinary system with varying degrees of discomfort. Stones that lodge in the ureter or renal pelvis grow in time to obstruct the flow of urine, and can become potentially life threatening.

Methods of Treatment

Removal of urinary calculi is a problem that has challenged the ingenuity of physicians for centuries. Three approaches have been recognized for removal of urinary stones: 1) open surgery, 2) closed surgery, and 3) chemotherapy. Closed surgery, which is the principal concern herein, was first practiced by the ancient Egyptian physicians [1] who devised a method to remove vesical stones by dilatation of the urethra with wooden probes. The closed surgery approach in later centuries was abandoned for open surgical procedures. However, in the late 18th century, interest rekindled in the transurethral approach to bladder stones. Angeloff [2] reported also that the Arabic physicians Albicosis of Cordoba and Avicenna performed blind lithotripsy. The first documented lithotripsy was, however, performed by Civiale in 1824. Since then many improvements have been made on the lithotripsy technique with the latest advance being the Electrohydraulic Lithotriptor (EHL). It was the preferred machine for the transurethral removal of bladder stones until a few years ago when the EHL invasive technique was replaced by the invention of the Extracorporeal Shock Wave Lithotriptor (ESWL), the only known non-invasive therapy. The ESWL approach was invented by Dornier System GmbH of West Germany in conjunction with a group of Urologists from Munich [3]. The method relies on the fact that the kidney stones can be made to fracture by a spalling-fatigue mechanism. This spallation can be produced in materials by the focused shock wave induced in water by the ESWL.

The ESWL technique relies on the fact that the spark generated shock waves are focused by an externally placed rotationally symmetric semi-ellipsoidal reflector onto the urinary calculus within the patient's body. The focusing of the shock waves is accomplished according to the geometrical property that the total length of the path from the first focus (F1) along any ray to the boundary and back to the second focus (F2) is constant, as shown in Fig. 1. Consequently, the reflected shock waves are in-phase. The sum of these reflected shock waves form a converging shock whose pressure magnitude increases as the pressure field converges toward the second focus of the reflector.

In current clinical procedure the patient, under general or local anesthesia, is suspended inside a water bath, as shown in Fig. 2. Orthogonal X-ray sources allow the physician to locate exactly the position of the stone with the help of two rubber balloons. The balloons are located as shown in Fig. 3, one on each side of the reflector in the tub. When they are inflated against the patient's back they act as a coupling medium between the body and the image intensifier of the X-ray system. Their function is to enhance the X-ray image on the monitors. The patient can then be positioned so that the stone coordinates coincide exactly with those of the second focal point or target (F2). Once correctly positioned, the heart is monitored and the breathing rate is suppressed to keep the stone stationary. The operation then starts by synchronizing the spark triggering rate at F1 with that of the heart beat rate. Because the characteristic impedance of

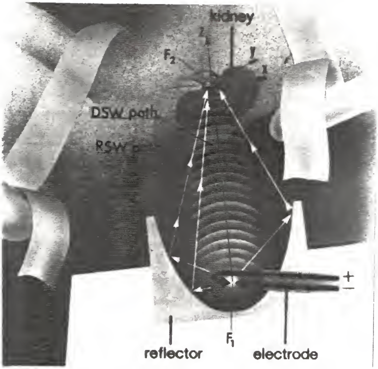

Fig. 1. Ellipsoidal reflector configuration.

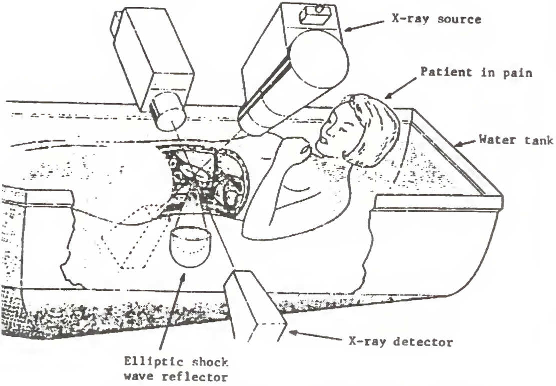

Fig. 2. Clinical lithotripter configuration (ESWL).

the coupling fluid and the tissue are almost identical, the shock waves propagate across the water-tissue interface with a little reflection. After several hundred shocks the stones will generally be broken and the resultant fragments are passed directly out through the ureter tube.

Previous Investigations on the Use of Spark Generated Shocks

For several years here at our institution (J. Hillis Miller Health Center), we have studied the fracture mechanism produced by Electrohydraulic Lithotriptor devices (EHL) [4]. We have made several studies recently [5, 6] using Extracoporeal Shock Waves generated by the Dornier Lithotriptor.

Underwater sparks have been used for many years as a spectroscopic light source. With a stored energy of several joules per discharge, the radiant output has a continuum in the ultraviolet which is useful for absorption studies. The underwater spark may also find application as a photographic light source of high brilliance [7], a subaqueous sound source [8], or a pressure source [9]. When the spark of sufficient discharge strength is produced under water by a rapidly discharging capacitor across electrodes, breakdown of the fluid occurs. This breakdown results in a rapid transfer of a large amount of electrical energy into a small volume spark channel. Also, the spark raises the temperature of the vapor within the channel sufficiently high so that a highly ionized, high pressure plasma is generated.

The spark initiated plasma tries to expand but the mechanical inertia of the surrounding water resists this expansion and this results in the development of high impact pressure or shock wave.

Water Breakdown

It has been established [10] that the electrical breakdown within the fluid is brought about by joining of the two streamers (leaders) of the electrode which move towards each other. The initial diameter of the spark is equal to the diameter of the streamer. A typical discharge circuit can be seen in Fig. 4. When the spark gap, S_g, is short-circuited, the voltage between the electrodes leads increases to a value of V_0. It retains this value for a time, t, which varies from the order of a fraction of a microsecond to tens of microseconds. The duration of the time, t, is most strongly affected by the shape of the electrode (sharpness), the initial voltage, and the spacing between electrodes [11].

To generate a high pressure plasma and a strong shock wave it is necessary to supply high power to the spark channel while keeping the spark channel volume small. This calls for a rapid rate of current rise and a high rate of energy liberation in the discharge channel. Skvortsov et al. [11] showed that the most important factor in the initial rate of discharge energy generation and shock formation is the rate of the current rise. Furthermore,

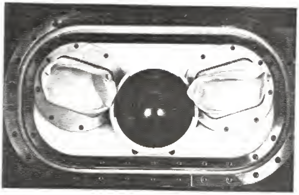

Fig. 3. The para-ellipsoid X-ray coupling balloons.

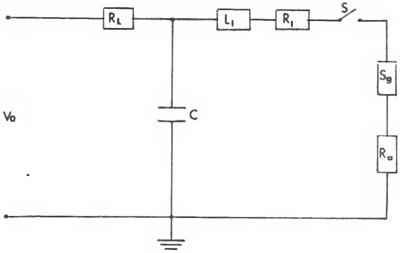

Fig. 4. Schematic diagram of the discharge circuit. (V_0: charging voltage, R_L: charge resistance, C_c: condenser, L_i: inner inductivity, R_i: inner resistance, R_a: load resistance, S: circuit spark gap, S_g: outer inductivity.)

increasing the capacity of the circuit by a factor of 2 while keeping the current constant does not cause any change in the energy generated. The dependence of discharge energy on the initial time derivative of the discharge current is linear and an increase in V_0 is accompanied by an increase in this energy. The same result is achieved by a reduction in the circuit inductance [11].

Dissipation of Energy

The discharge plasma exhibits such a large capacity for storing energy in the form of dissociation, excitation, ionization, and kinetic energy of random motion of the constituent particles, that most of the electrical energy input to the spark is stored within the discharge channel [12]. The particle density in the channel is great enough so that the radiation emitted, ionization and dissociation can be neglected [12] relative to the plasma kinetic energy. In addition, the energy loss in the circuit is small, particularly during an aperiodic discharge and usually not more than a few percent of the energy stored in the capacitors ($W = 0.5\ C_t V^2{}_0$, where C_t is the circuit capacitance). It should be noted here that the dissipation of the energy in either the water or the circuit between the electrode spark gap and the pressure gage is not easily measurable.

Focusing of Shock Waves

In recent years there has been considerable interest in focusing shock waves at smooth caustics as a result of reflection or transmission from curved boundaries. In his theory of shock dynamics, Whitham [13, 14] has described the behavior of shock waves of moderate strength. An important experimental study of these phenomena in air has been done by Sturtevant and Kulkarny [15]. The focusing of weak shock waves at caustics has been described analytically by Hayes [16] and by Pechuzal and Kevorkian [17]. Cramer and Seebass [18] have examined the focusing of weak shock waves at two dimensional caustics. Ting and Herrmann [19] studied the propagation of a shock wave front through a lens-shaped elastic body.

Much work has been carried out on stress wave reflection from flat boundaries. Studies concerned with fractures due to stress wave focusing is rather meager. Several investigations have reported on the effect of stress wave focusing [20, 21, 22, 23]. Chaussy et al. [24, 25] used a semi-ellipsoid to focus shock waves for the purpose of fracturing kidney stones, but the physics of the process by which this occurs was not discussed. Also, Al-Hassani and Gomes [26] studied the internal fracture mechanism produced by stress waves focused by paraboloid of revolution without studying the characteristics of these waves.

Cavitation Phenomenon

It is well known that cavitation damage is attributed predominantly to an impact pressure produced by a collapsing bubble. In order to clarify the mechanism of the impact pressure generation, many studies were done on the bubble dynamics [27-43]. Two factors were found to be predominant in generating the impact pressure. One is a liquid jet developed from the instability of a collapsing bubble, and the other is a shock wave generated at the instant of the rebound of a bubble. Recently Fujikawa and Akamatsu [32, 33] showed that an impulsive pressure accompanying the bubble collapse was caused by the impact of shock waves. In addition, the jet impingement did not produce any detectable effects. Shima et al. [36] reconfirmed the generation of shock waves during the rebound of spark bubbles. They also observed the coexistence of a shock wave and a liquid jet in the case where a bubble almost touched a solid wall at its maximum expansion.

In theory, a liquid will vaporize when the pressure is reduced to its vapor pressure or when the temperature reaches the vaporization point. In practice, the pressure at which cavitation starts is greatly dependent on the liquid's physical state. If the liquid contains much dissolved air, then as the pressure is reduced the air comes out of solution and forms cavities in which the pressure will be greater than the vapor pressure of the liquid. Even if there are no visible air bubbles, the presence of submicroscopic gas bubbles may provide nuclei which cause cavitation at pressures above the vapor pressure. Each cavitation bubble grows from a nucleus to a finite size and collapses again, the entire cycle takes place within a few milliseconds. In the absence of nuclei, the liquid may withstand negative pressure or tension without undergoing cavitation. In theory, a liquid should be able to withstand tension equivalent to thousands of atmospheres. It is estimated that water will withstand a tension ranging from 500 to 10,000 atmospheres [42]. In practice, even when water has been subjected to rigorous filtration and prepressurized to several hundred atmospheres, it has ruptured at tension of 300 atmospheres [43].

The cavitation "microbubble paradox" refers to the fact that experimental values of underpressure or superheat necessary to provoke bubble nucleation are generally at least an order of magnitude less than the theoretically predicted values of liquid tensile strength would indicate should be the case, even though extreme care is taken to degassify and purify the liquid. Thus, the existence of stabilized gas or vapor microbubbles or, conceivably, unwetted solid particles must be postulated to explain the observed nucleation threshold values.

In an experiment to study the imposed pressure oscillation on a water medium, Hammitt [41] found that if water is carefully filtered to remove solid particles down to an arbitrarily small size and is also well deaerated so that any entrained gas bubbles will either quickly go into solution or rise to the surface, there is then no apparent mechanism for the persistence of nucleation centers. Similarly, long setting time water will help very small bubbles to dissolve and larger bubbles to rise to the surface by buoyancy effects. In such experiments it is invariably found that the pressure oscillation magnitude is much less than would be expected if full pure-liquid tensile-strength values were realized.

When the cavities collapse, high pressures and temperatures are produced in the fluid surrounding such bubbles. The temperatures reached can be as high as 10,000 K [43]. Wheeler [40] has concluded that temperature rises of 500 to 800 C can occur in the material adjacent to the collapsing bubble. The high pressure, on the other hand, has been estimated based on the energy in the radiated pressure wave produced at the end of the bubble-contraction phase. When not considering the dissipation of the energy, it should be no surprise that the theoretical results of the bubble pressure are qualitatively useful rather than quantitatively reliable. A heavier burden is therefore placed on experimental investigations in evaluating the phenomena.

ESW as a Fracture Mechanism

Recently we examined the efficiency of the ESWL technique in terms of concretion fragment size as a function of position along the shock wave path [6]. In this study we used simulated stone material referred to as "Z-brick," a square piece of frontal area of 1 cm^2 subjected to 300 shocks. However, the fracture patterns and the generating stresses were not examined. As a continuance of this work, we have studied the fracture of shock-tested urinary concretions along the shock propagation direction.

CHAPTER II

EXPERIMENTAL APPARATUS AND PROCEDURES

The underwater shock wave generated by a single short duration spark within a semi-ellipsoidal reflector is a phenomenon which can lead to more than one impact fracture mechanism for the crushing of kidney stones. The dominant of these mechanisms, namely shock wave impact and the accompanying cavitation bubble collapse, are the topics of investigation in this dissertation. We also used such shocks to test simulated urinary calculi and examined the resultant fracture patterns.

Before carrying out our experimental investigation, we first briefly described the needed equipment and its properties pertaining to our experiments.

Listing of the Experiment Equipment

The equipment used in our experiments can be grouped into two classes: i) the major components include the Extracorporeal Shock Wave Lithotriptor (ESWL), the Electrohydraulic Lithotriptor (EHL), test chamber, rotationally symmetric ellipsoidal reflectors, lights, spark electrodes and mechanical clamps; while the recording components

ii) include a Data 6000 main frame with 620 Plug-In Digitizer, a dual disk drive, pressure transducers, vomputer, a Material Testing System, high dpeed movie and still types of cameras.

Features of Some Individual Components

Extracorporeal Shock Wave Lithotriptor (ESWL) The Dornier-made ESWL [3], which the University of Florida Medical Center has used, is one of thirteen machines owned by Uro-Tech Co. in this country. The ESWL consists of a padded metal palette which is hoisted slowly off the floor by an overhead crane and positioned by a conveyor just above a stainless steel tub of water. Straps are used to secure the patient with kidney stone to a stretcher. The frame on the gantry can be adjusted via a hydraulic drive to the desired angle to help position the patient correctly within the tub.

Two large X-ray tubes, shown in Fig. 5, one mounted on each side of the tub, are swung inward and placed gently near the patient's flanks; two television monitors reveal the stone.

To adjust the stone position to a precise spot in the tub, the palette carrying its passenger is moved until the stone is centered at the cross-hair of the two X-ray images displayed on the TV screen monitors shown in Fig. 6.

By using a button on a hand-held remote control device, a spark can be triggered at the electrode located at the first focus of the semi-ellipsoid at about one second intervals, leading each time to the creation of a spherical shock. A digital counter on the console shown in Fig. 7, records the number of shots taken during the operation. The spherical shocks are focused by the ellipsoid reflector built into the tub. Such focused shock waves impinge on urinary concretions without major damage to the surrounding soft tissue.

ESWL Spark Electrode

The electrode used in the spark triggering mechanism of the ESWL is made of steel rods 4 mm in diameter, having tungsten tips with a taper of 25 degrees. The steel rods were isolated from the rest of the device by synthetic material as shown in Fig. 8. The electrode separation can be altered from the original spark gap of 0.4 mm and can increasingly vary with the number of triggered shocks.

Electrohydraulic Lithotriptor (EHL) Stone Disintegrator (Wolf)

The EHL shown in Fig. 9 consists of an electrical circuit which transforms the standard AC to high voltage, low amperage direct current which is used to charge a high capacity condenser bank. The condenser is connected to an electrode located at the first focus of the ellipsoid reflector. A typical electrode is shown in Fig. 10. It consists of an inner insulated wire conductor and an outer ring-shaped conductor. A second layer of insulation surrounds the entire electrode. Via a switch located on the

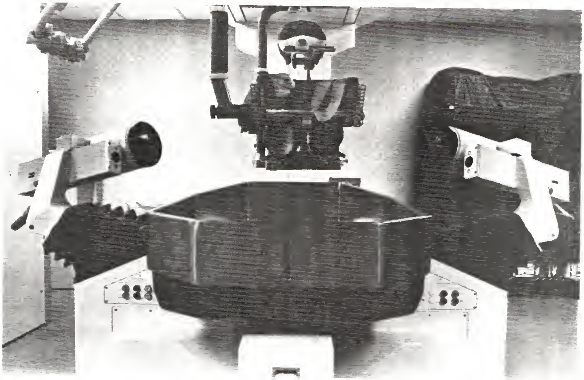

Fig. 5. The extracorporeal shock wave lithotripter (ESWL).

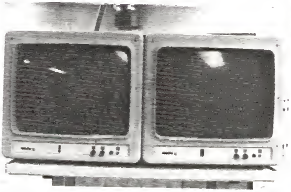

Fig. 6. TV screen monitors.

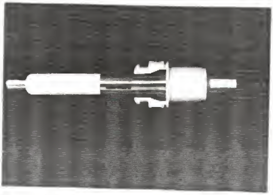

Fig. 8. The spark electrode of the ESWL.

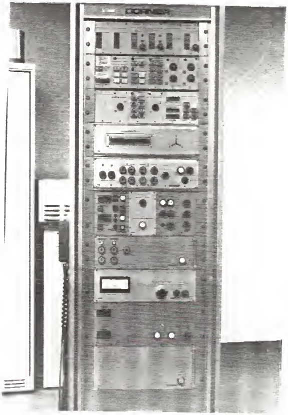

Fig. 7. The control unit of the ESWL.

panel, the discharge of the capacitor bank across the electrode tip can be altered. The experiments were performed at the maximum voltage of 10 kV. It should be noted that the circuit can trigger a single or multiple electric discharge at different power levels and pulse durations. Through the resultant spark, a hydrodynamic shock wave is created which is focused via a machined ellipsoidal reflector.

Shock Interactions Test Chamber

The test chamber experimental setup shown in Fig. 10 consists of an aquarium made of plexiglas to allow direct observation of the phenomenon. The chamber (Fig. 11) was designed large enough (1' x 2.5' x 2.5') and of sufficient wall thickness (1") to dissipate any residual stresses in the water. On the sides of the chamber walls there were mounted metal reflectors in such a way that two identical ellipsoids were positioned facing each other and adjusted to share the same target focus (F2). The third reflector in the form of a paraboloid was attached to the longer side walls. The ellipsoidal reflectors were used to focus the initial spherical shock generated by the EHL probe at F1, presumably, to a point along the reflector vertical symmetrical axis, while the paraboloid reflector was made so as to generate a beam of plane shock that can be focused by an acoustic lens. The metal reflectors were designed by computer and machined by CNC lathe machine to insure

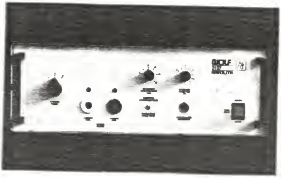

Fig. 9. The electrohydraulic lithotripter control unit (EHL).

Fig. 10. The spark electrode of the EHL.

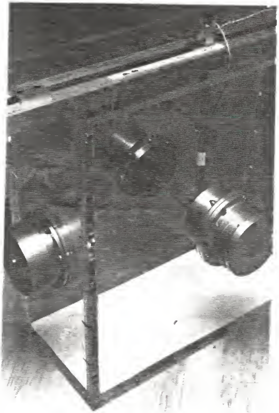

Fig. 11. Test chamber experimental setup.

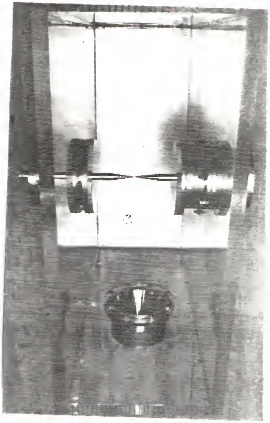

Fig. 12. Reflectors configuration on test chamber.

accuracy and rotational symmetry around the major axis. Each ellipsoidal reflector was manufactured from stainless steel and designed such that its major semi-axis is 14 cm and the minor semi-axis is 7.98 cm, typical Dornier ellipsoid dimensions. The stainless steel was selected over brass because of its higher characteristic impedance. That high characteristic impedance helps reflect a higher percentage of the impinging shock energy back into the reflected shock. In addition, the stainless steel material does not tarnish and hence will not distort the focusing quality of the shock wave and also will not weaken the shock strength.

EHL electrode positioning devices such as pins and caps were designed and manufactured in such a way that it enabled us to locate the geometric foci (F1, F2) and consequently, helped us make accurate measurements.

Mechanical Holders and Clamps

Three different types of holders and clamps were used in our experiments. One was used in the experiments made on the ESWL with and without a clamp, which enabled us to hold the simulated urinary stones in the tub. Another was used in the shock interaction test chamber with an arm designed to hold and move a pressure transducer around within the chamber.

Mechanical Holders Used in the ESWL

A rigid aluminum holder was designed to be attached to the gantry (patient positioning device). At the end of that holder, an arm made of stainless steel was pivoted through a slot. The arm was adjusted to incline at any angle up to 90 degrees to the holder vertical position as shown in Fig. 13. In addition, the arm was made so slender that it could move in the tub freely without occupying much space. That enabled us to position easily the transducer which was fixed in a block at the end of that arm. It should be noted here that the reflected pressure field is inclined at 14.28 degrees to the vertical direction (the reflector inclination angle to the vertical position).

The test concretions were held by another clamp manufactured of steel, and attached to the very end of the arm where the transducer block was held, as shown in Fig. 14.

Mechanical Holders Used in the Test Chamber

On the top of the test chamber there was fixed a mechanical holder (Fig. 11) with a built-in positioning device. That holder was attached to a zigzag shaped arm made of steel (Fig. 15). The setup was designed not only to hold the transducer but also to move it to any point within the chamber. That transducer was fixed in a block fixed to the arm by which the transducer can be adjusted to move linearly and angularly in three dimensions.

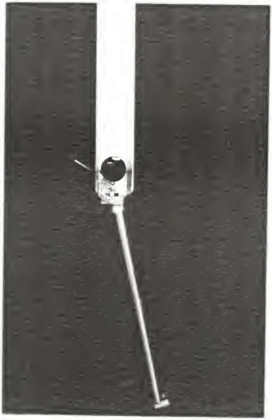

Fig. 13. Mechanical holder in ESW.

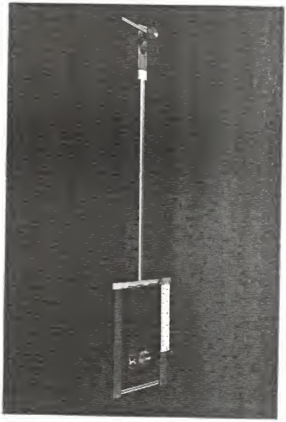

Fig. 14. Clamp for test concretions.

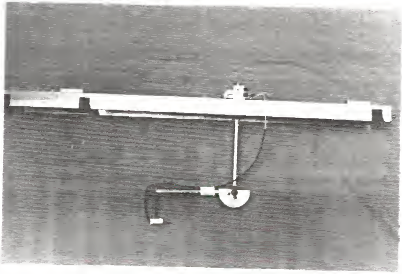

Fig. 15. Mechanical holder of EHL test chamber.

Digital Storage Oscilloscope

A universal wave form analyzer manufactured by Analogic-Data Precision consists of a Data 6000 main frame and 620 plug-in module with two channels. The Data 6000 (Fig. 16) acquires an analog signal, digitizes it, stores each sample value in a temporary "Frame," and when the frame is full, transfers the frame data into a "Buffer." The buffer record is then used as a source for display and/or calculations. The plug-in module rise time is 20 nsec and can sample at the high rate of 10 nsec per point. The trace can be as long as 30000 points depending on the sampling rate used. The main frame built-in computer allows almost any mathematical and statistical programming through the front panel push-button set of keys. It can be interfaced to a dual disk drive and a plotter in addition to a computer for more complicated manipulations.

Material Testing System (MTS)

The material testing system was manufactured by MTS System Corporation and designed to be versatile, to have a wide range of capabilities, and to allow quick setup changes of specimens or production materials. It consists of a hydromechanical device and an electronic circuitry housed in the control unit (Fig. 17). These systems applications include large computer controlled servohydraulic materials and structural testing systems. It can be used for specimen

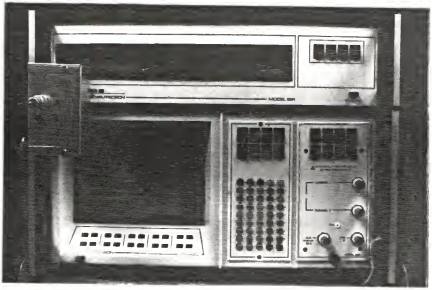

Fig. 16. Wave digitizer, Data 6000.

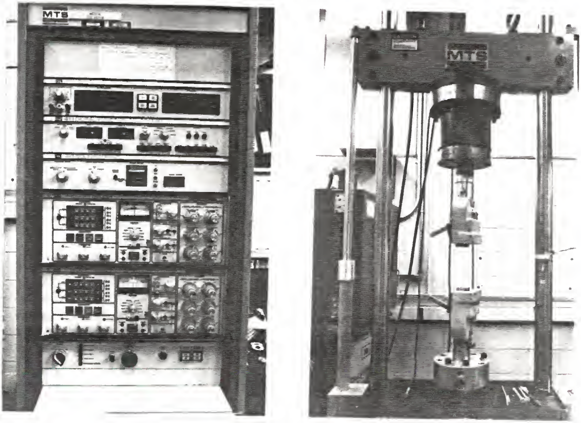

Fig. 17. Material test system, control unit and hydraulic unit for stress-strain tests.

failure testing in shear, bending, tension and compression. It consists of a control unit and the testing arms that can accommodate clamps or grips for holding the specimens. Through the control unit, the mode of testing and the rate of loading are adjusted as well. The output can be in the form of stress or strain. It can be either read off a digital panel of the control unit or plotted on paper via an attached plotter with a different setup feature to accommodate the signal.

High Speed Movie Camera

A Nova model 16-3 16mm high speed movie camera (Photokinetics, Inc., Poughkepsie, N.Y.) was used. This camera consists of a continuously moving film strip, and employs a rotating prism as optical compensator and shutter. The camera speed is from 10 to 10000 frame/sec using a standard 16mm rotating prism. For applications requiring more than 10,000 frames/sec, various prism assemblies are available. A full frame prism was used in the present study to obtain photographic data at speeds up to 7500 frame/sec. An accessory 400-foot magazine was attached to the basic camera body in order to accommodate a 400-foot Kodak 4-X Reversal Film 7277 film (Eastman Kodak Co., Rochester, N.Y.). The film used can be processed by normal commercial producers and expanded in order to obtain photo reproductions. The set-up of the camera assembly, including a power supply is shown in Fig. 18. The still pictures were taken with Canon F-1 with

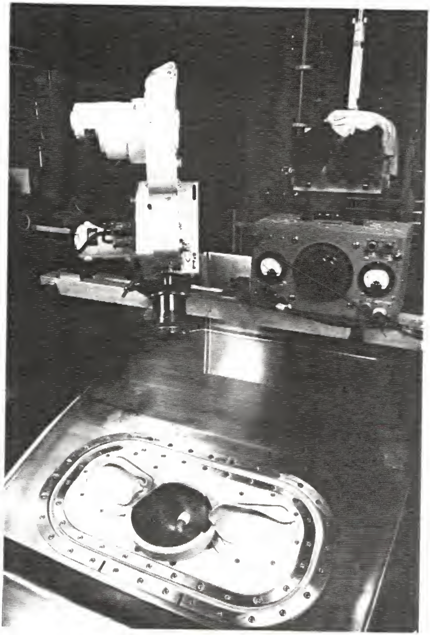

Fig. 18. High speed movie camera setup.

50mm f/3.5 macro lens using Panatomic-X (Pan-X), ASA 32 film. Also, a motor drive (power winder) 5 fps and an extension tube were used.

Pressure Gauges Desired Specifications

In the present experiment, the shock wave is extremely transitory and as a result the transducer and the associated electronics must have a faster rise time than the phenomenon being recorded in order to avoid any additional errors in measuring the pressure. The upper pressure ranges are expected to be of the order of 1 kbar. Furthermore the strength and the curie temperature should be high in order to allow a long life time. In addition, linearity, reproducibility and high sensitivity should be a major feature of the pressure transducers to be used.

Practical Problems with Commercial Transducers

Commercial transducers that are available on the market for use in under-water experiments are not faster in response than 1 microsec. In addition, the sensing element of the commercially available transducers (usually a piezoelectric ceramic, quartz, or tourmaline) is not designed for impact experiments. A model 109A transducer (Fig. 19), made by PCB Co., N.Y., was used in our first study [5]. The transducer is basically made of a quartz crystal of about 1 microsec rise time and an upper pressure range of

5.5 kbar. This was not satisfactory for our measurements because the rise time was slower than that of the input signal which was presumably of the order of nanoseconds. This means that such a transducer will yield a signal which does not represent a true pressure-time reading for the shock wave. Furthermore, the impedance mismatch "ceramic cover and air environment," which the shock wave propagates through before reaching the sensing element, makes the signal noisy and affects the signal magnitude. Therefore, the error on the output signal was considered significant. A modified version of another transducer, namely version 138MO6 (Fig. 20), was made by the same company for use in our experiments. The crystal was made of tourmaline and was designed to be hung on two wires which were connected to an amplifier of less than a microsec rise time.

After field testing, the transducer turned out to be not satisfactory because of the transducer's low sensitivity in addition to its short life time. A common problem was that the crystal loosens from the suspended wires after the shock wave impinges several times. After further modification, such as using a sheath of tygon tubing to house the crystal as shown in Fig. 21 and later using a signal conditioner to cut down on the noise received and enhance the S/N ratio, we abandoned the use of this transducer. We concluded at that time that we had to custom produce a transducer tailored to fit our experimental requirements.

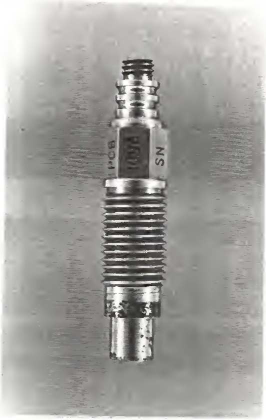

Fig. 19. Pressure transducer PCB-109A.

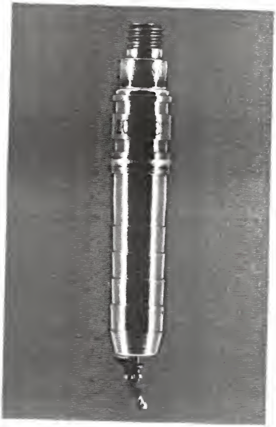

Fig. 20. Pressure transducer PCB-138MO6.

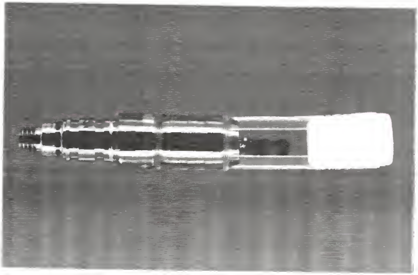

Fig. 21. Pressure transducer, modified version PCB 138MO6.

Piezoelectric Crystals

In the almost one hundred years since the piezoelectric effect was discovered, the phenomenon has been used in a number of devices for a wide range of applications.

A piezoelectric material is one that changes its length when an electric voltage is placed across it. In the process of trying to change its length, it can exert a force on anything that tries to keep it from changing its length, such as the inertia of some structure that may be in contact with it. The converse effect is also true for these materials; if they are forced by mechanical means to change their length, a voltage or a current appears across the piezoelectric material. A magnetostrictive material behaves the same way [44], except that the material produces a magnetic field around it in the former case and is sensitive to a magnetic field instead of an electric field in the latter case. All magnetic materials are magnetostrictive.

There are two general classes of piezoelectric materials: those that are naturally piezoelectric and those that are piezoelectric only after they have received special treatment which causes them to become polarized and show piezoelectric properties.

One way to visualize the piezoelectric effect is to consider that each of the individual unit cells in a crystal contains a dipole. A dipole results from a difference between the average location of the positive charges and the average location of equal negative charges in a unit cell.

If a crystal composed of identical unit cells, each of which has a dipole, is squeezed or stretched parallel to the direction of the dipole, electric charges will appear on the opposite end-surfaces of the crystal. Conversely, if the electrodes are placed on these same surfaces and a voltage is applied to them, the dipoles, and hence the crystal, will lengthen or shorten, depending on the polarity of the applied voltage, because of electrostatic attraction or repulsion. Natural or artificially grown piezoelectric crystals are inherently composed of perfectly aligned dipole cells. Electrostrictive materials have had the dipoles put into them by means of a polarization treatment. The electrostrictive effect is merely the elongation that all dielectric materials undergo when they are placed in an electric field. Some materials, such as ferroelectrics, show this effect more than others. The magnitude of the effect is proportional to the square of the applied field, and hence an elongation of the material may always occur for either a positive or negative applied field. Polarization of ferroelectric materials is accomplished by heating them to a temperature above the curie point (the temperature at which the magnetostrictive or electrostrictive effect disappears) and then allowing them to cool slowly in an electric field of about 30,000 volt per inch which is oriented in the direction in which the material is to be excited piezoelectrically.

Piezoelectric crystals have orderly three-dimensional structures, which affect the quantity of charge generated at the sample surface when stress is applied in specific directions. For a given direction of stress, the charge generated per unit area by the internal polarization is usually directly proportional to the applied stress or strain. The constant of proportionality, called the piezoelectric constant, depends upon the crystallographic direction in which the charge is detected [45]. A piezoelectric can have as many as eighteen piezoelectric constants to define polarization measurements in any three directions for three different measurements of both normal stress and shear stress [46]. Thus, the piezoelectric response of a transducer will depend markedly on the direction in which the active element is cut from the crystal.

Selection of Sensing Element Material

Although many different crystals generate piezoelectric charges when they are compressed, quartz has been used as the active element in most piezoelectric applications since it has high stability, high electric and tensile strength; however, it requires relatively high electric field strength to obtain high power outputs [47]. On the other hand, the polycrystalline ceramics possess much higher dielectric constant values and require much lower electric field strengths for equal power outputs from the same size area.

They have the disadvantages of lesser stability than quartz, higher internal losses and electrical input impedance too low at high frequencies. Accurate reproducibility is better with quartz, but if it is not essential, ceramic may be used [48].

Common orientations for quartz sample "cuts" are x-cut, y-cut and z-cut with respect to the crystal axes. A Lithium niobate crystal, on the other hand, has four piezoelectric constants, whereas quartz has only two. In addition, it exhibits a piezoelectric response to uniform hydrostatic pressure, whereas quartz does not. Furthermore, it possesses very large piezoelectric coupling coefficients, several times larger than quartz and very low acoustic losses. Because of its Curie temperature of 1150° C, it can be utilized as a high temperature acoustic transducer. It also possesses a number of useful cuts which are now used in transducer applications. Two compressional cuts are popular, the z-cut and 36° rotated y-cut. The shear mode cuts most commonly used are the x-cut and the 163° rotated y-cut. Because of its high efficiency, broad bandwidth capability, low dielectric constant for all orientations, consistent repeatability, problems associated with signal-to-noise ratio at low stresses can be reduced particularly with small gages. After reviewing numerous studies on piezoelectric crystals and their properties, Lithium Niobate was chosen as the best material for our experiments. Graham [49] showed that the piezoelectric responses of lithium niobate were reproducible and of high sensitivity. In addition, the output nonlinearity was found to be 14% per GPa. In addition, several investigators [50, 51, 52] recommended it for stress transducers particularly in impulsive loading measurements. Furthermore, it has a larger piezoelectric stress constant than that of quartz. This means that the signal gain is more than that of the quartz at the same input stress. In addition, Lithium niobate will be more useful for low amplitude stress measurements [50].

Transducer Mode

It is important to explain some factors which play an important role in the piezoelectric transducer operation. Piezoelectric transducers for measuring stress or pressure pulses are used in either of two modes, the current mode or the charge (voltage) mode. The selection of the mode depends on the input signal characteristics. The current mode is used for measurement of the stress-time characteristics of fast-rising stress impulses and requires circuits with short electrical time constants, and gages that are thick compared to the stress impulse length. In this mode the measurable pulse durations are less than transit times of stress pulses through the gages. On the other hand, the charge-mode of operation is used for the measurement of the stress-time characteristics of stress pulses of long duration and requires circuits with long electrical time constants and gages that are thin relative to the widths of the stress pulses. In this mode the measurable rise-times are longer than the transit times of the stress pulses through the gage.

Transducer Calibration

Sigrist [53] has cited a theoretical transducer calibration formula derived by Meier. The governing formula was based on short circuited electrodes and additional simplifying assumptions. Among these assumptions is that the pressure front is parallel to the electrode disk face. Meier generalized the solution to the problem for four different cases. These cases can be distinguished with respect to the signal duration, T_s, the acoustic transit time through the crystal disk d/v and the electrical time constant RC_t of the system. However, since our measurements are based on free field stress waves in water, the element is in constantly varying equilibrium with the surrounding medium; therefore, recording must be in the open mode. Hence, the differential equation and its solutions developed for the measured voltage signal U(t) has to be modified. As a result, we simply replaced the piezoelectric factor in the stiffened charge mode by the hydrostatic piezoelectric constant. The former is a ratio of the piezoelectric constant with constant stress to the elastic stiffness constant (the modulus of elasticity). The hydrostatic piezoelectric constant is termed the hydrostatic strain coefficient. The transducer geometry has undergone some changes, namely the crystal is set free in the testing field. However, the equivalent circuit used for the derivation of the corresponding equations was kept the same as shown in Fig. 22. Under these conditions the Sigrist [53] equation transfers the electric potential U(t) as follows:

$$\frac{dU(t)}{dt} + \frac{1}{RC_t}U(t) - \frac{HAV}{C_t d} \cdot [P(0,t) - P(d,t)] = 0 \tag{1}$$

where: H = The hydrostatic piezoelectric constant

v = The sound speed within the crystal

A = Disk area

C_t = The total circuit capacitance

with solutions which can be expressed as follows:

$T_s < \frac{d}{v}$

$RC_t << T_s$ $$U(t) = \frac{HARv}{d} P(0,t) \tag{2}$$

$RC_t >> T_s$ $$U(t) = \frac{HAv}{C_t d} \int_0^t P(0,t')\,dt' \tag{3}$$

$T_s > \frac{d}{v}$

$RC_t << T_s$ $$U(t) = (HAR)\frac{dP(0,t)}{dt} \tag{4}$$

$RC_t >> T_s$ $$U(t) = \frac{HA}{C_t} P(0,t) \tag{5}$$

Reed [52] has also theoretically calibrated Lithium Niobate as an impact transducer; however, the derivation and treatment of the problem was different from Meier's. Limiting the problem to a specific case where $RC_t >> T_s$ and $T_s > d/v$, he simplifies the solution under the condition that a variation of charge is measured in response to changes in the forcing variables. The reference state is for a charge-free element at ambient zero stress conditions. For free field stress measurements, no electric field is imposed and temperature is presumed to be essentially constant. The final form written below agrees with the modified version of Meier's solution.

$$U_i = \left(\frac{Ad_{ij}}{C_t}\right) T_j \tag{6}$$

For a normal stress component along the z-cut of the crystal i=j=3

$$U_3 = \left(\frac{Ad_{33}}{C_t}\right) T_3 \tag{7}$$

In the hydrostatic case $T_3 = P$ and $d_{33} => H$

$$U_3 = \frac{AH}{C_t} \quad P \tag{8}$$

where

T_j = the stress applied along the j direction

P = pressure.

The Meier solution is much more specific and therefore we intend to use this modified version. In our case we had

$RC_t > 1$ ms,

$T_s < 10$ microsec, and

$d/v < 80$ ns,

thus; $RC_t \gg T_s > d/v$.

According to eq. (5), the voltage signal U(t) is proportional to the pressure amplitude P(0,t) incident on the front face of the piezoelectric disk.

The sensitivity is given by $\frac{C_t}{HA}$ and the response time is defined by $\frac{d}{v}$.

Higher sensitivity could easily be achieved by using larger electrode areas. However, Meier cited that if the pressure fronts are of hemispherical geometry the assumptions for the derivation of the equations above, namely the parallelism of the pressure front and the disk electrode, could not be fulfilled when using large disks. In our case, where the pressure front of the focused shock wave was a plane of finite size, we had no problem using a relatively large size disk.

Design Characteristics of the Transducer

The transducer was custom-made by Specialty Engineering, San Jose, CA. It is basically a Z-cut of a quarter inch diameter Lithium niobate crystal and one-tenth of an inch thick, as shown in Fig. 23. That ratio has been recommended by Halpin et al. [54] as it minimizes both the added polarization resulting from unloading waves propagating inward from the lateral boundary and the peripheral electrical fringing producing distortion of the signal. In addition, Graham et al. [55] suggested that this geometry is a means to ensure one-dimensional strain in the gauge. Murri et al. [56] also cited that it is required that the diameter to thickness ratio be of order 5; however, it is preferable that the ratio be 10.

The transducer electrode configuration also is one of the factors to be considered in building a transducer since the variation of the frequency constants of the fundamental resonance as well as antiresonance are functions of rotation angle around the crystal X, Y and Z axes. In using a thickness mode, the fabrication requirements of the sensing element are reduced to achieving flatness, smoothness and parallelism and orientation of only the major faces of a sample. Moreover, thicker plates could be operated on high overtones, while the thinner plates gave better freedom from unwanted modes at the fundamental and low overtone modes [57].

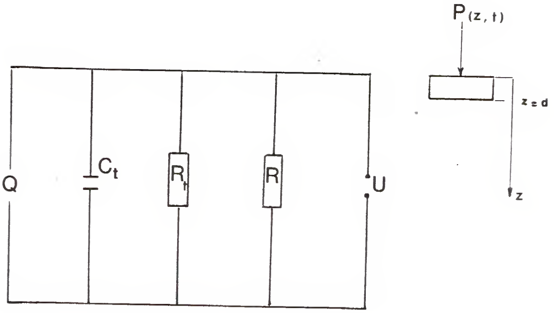

Fig. 22. Equivalent circuit of the hydrostatic (custom made) pressure transducer. (Q(t): induced charge, C_t: total capacitance, R_t: Resistance of transducer, R: Input impedance of oscilloscope, U(t): measure voltage signal, P(Z,t): pressure amplitudes.)

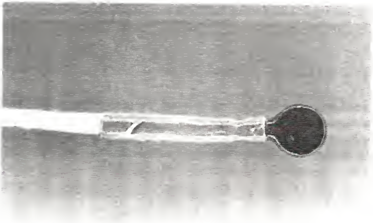

Figure 23. The hydrostatic pressure transducer.

The electrodes used were gold, deposited directly on the crystal plates by evaporation in a vacuum of about 10E-4 torr on both sides and then coated with silver conductive paint after attaching No. 30 wire to it.

Experimental Procedures

Our goal is mainly to determine the characteristics of the spark induced-hock phenomena and their intensity at points along the Z axis of the ellipsoidal reflector, mainly in the ESWL.

The measurements in the ESWL were made in a stainless steel tub which can be filled with preheated, degassed and softened water via the lithotriptor water treatment unit.

The water specifications for ESWL operation are tabulated in Table 1.

Table 1. Coupling Fluid Conditions.

Flow rate	2 m^3/h
Temperature	32 - 40 C
Overpressure	2.5 - 4.5 bar
Residual gas content	max. 0.5 g/m^3
Water hardness	max. 0.5 dH

The measurements were made along the Z axis connecting the two foci of the ellipsoid reflector (Fig. 1) using electrodes with a spark gap, S_g, of 0.4 mm to 2.25 mm, keeping the para-ellipsoid X-ray coupling balloons in the deflated mode. The input voltage and the water temperature were adjusted to be 20 kV and 30° C, respectively. The water within the tub was always kept deaerated. The X-ray alignment apparatus was checked and found to determine accurately the location of F2 via cross-hairs. All the experimental runs were performed with the fast response Lithium niobate pressure transducers described above and custom-made by Specialty Engineering, California. The transducer's signals were fed into a digitizer via a shielded cable in order to lower the noise-signal ratio of the output. Calibration of the pressure transducers were done independent of the manufacturer, and hence reproducibility was assured.

The pressure transducers were fixed in a home-made mechanical fixture. To correctly position the transducer, the clamp was fixed on a gantry which can give a spatial positioning in three dimensions (X, Y and Z) within the tub to an accuracy of 1 mm in each direction.

Since the coordinate axes system of the gantry is different from that of the ellipsoid reflector, we developed a software program to convert the gantry coordinates into the reflector coordinates with a nominal accuracy of 1 mm in each direction. After adjusting the transducer at the second focus (target point) fluoroscopically or by using the adjusting tools (cap and pins), the F2 coordinate point can be read off a digital panel on the control unit and then used to calculate any set of points in the shock wave field to which the transducer is moved. Signals from the transducers were recorded and stored on floppy disks for later analysis.

It will be shown in the next chapters that there is generally more than one fracture mechanism along the Z axis, namely, direct shock wave (DSW), focused shock wave (RSW), cavitation formed at the first focus (F1) and cavitation formed at the second focus (F2). However, the most important fracture mechanisms expected to be directly involved in the urinary stones crushing process are the mechanisms which have a direct impact on the concretions positioned at F2.

The characteristics of focused shock waves (RSW) and the direct shock waves (DSW), including both the temporal and the spatial distributions of the pressure, the shock impulse, energy flux density, velocity of propagation, rise, time, and duration were measured. But before that, it was of higher priority to gain an insight into the individual influences of a number of parameters pertaining to the ESWL itself, on the efficiency of the RSW used in crushing kidney stones and its focusing quality in terms of the spatial range over which the pressure falls off considerably from its value at the focal point.

Because of the inhomogenity of the urinary stones, the strength, accordingly, varies considerably with not only its chemical composition but with its physical structure. Urinary calculi have been modelled therefore in terms of their compressive strength in order to study the fracture mechanism of such concretions as a function of the number of shocks and concretion position along the shock wave path.

Sample Preparation

The simulated stones were made of Gypsum cement, (Ultracal 60, manufactured by United States Gypsum) in two forms, namely, those of low strength and those of high strength. Both the low and the high strength concretions were made by mixing gypsum cement with water and letting the mixture set and age with time. Both kinds of samples were left to dry in air in order to slow down the chemical reactions and consequently slow down the gain in strength.

The mixing process of the gypsum and the water was initially done by hand, but after testing some samples of the same batch, we found that the strength varies considerably. Therefore, we had to change the mixing process. A rotating hand mixer was accordingly used and the time of mixing was also maintained constant through the overall process.

The samples were formed in a cylindrical shape. This shape allows us to study the interaction of the shock wave with both a flat surface and with a curved surface. The samples were, as big in size as mid-size urinary stones, of typical diameter of 2 cm and a length-diameter ratio of 0.5

to 1. It was necessary that the samples were free of voids in order to allow reproducible measurements. A releasing agent (mineral oil) was used in order to separate the cast simulated concretions from the molds without damaging their surface.

The required compressive strength which the samples have to withstand is about 180 atm. for the hard stone model calculi and 65 atm. for the soft stone model calculi [58]. To achieve such a compressive strength, we varied the amount of water and the age of the sample keeping the other parameters constant. The failure stress was monitored using the MTS equipment. It should be mentioned that the dry density was measured since the strength varies with compaction and consequently with the mixture density.

It is expected that spalling or scabbing will occur as a result of the transmitted wave which is reflected at the opposite side of the material with a phase reversal relative to the incident wave. The subject of spallation and scabbing due to stress reflection is well documented in the literature [59] and therefore it will not be discussed in detail.

Compression Tests

Compression tests were conducted on the urinary test concretions and a load-displacement curve was recorded for hard type stone models as shown in Fig. 24.

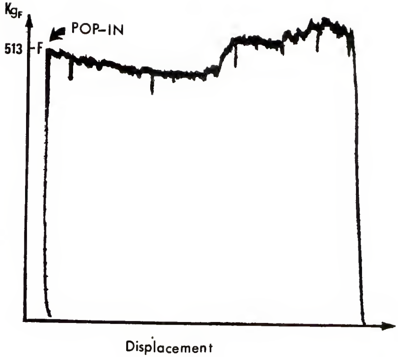

Fig. 24. Static (quasi-static) compression test of urinary test concretions.

Three specimens were tested under the same conditions. The specimens show almost reproducible deformation behavior. In Fig. 24, the curve rises linearly and smoothly, representing the elastic behavior of the specimen. When the loading reaches a certain value F, the first load drop or so called "pop in" occurs. This load drop indicates the unstable growth of a microcrack in the specimen.

As the loading continues beyond F, the specimen deforms more and more due to microcracks, densification, closure of pores and possibly some plastic deformation occurring until failure of the material.

The compression strength is defined at the first load drop. Fig. 25 shows the specimens' compressive strength as related to the dryness time and the material composition.

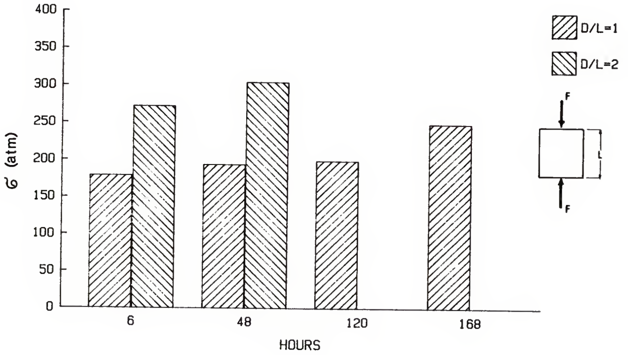

Fig. 25. Correlation between the compression strength of test concretions and dryness time for two cylindrical model configurations mixed at the ration a) W/G = 1/3.

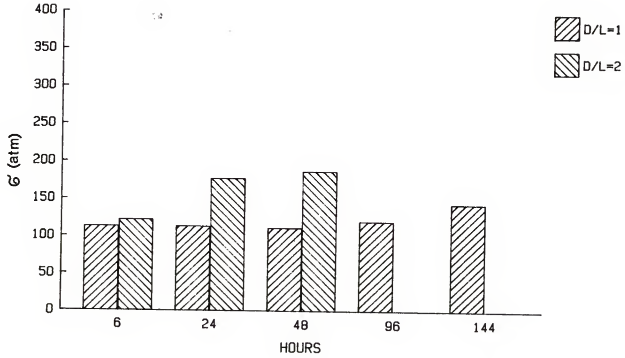

Fig. 25. Continued.
b) W/G = 1/2.

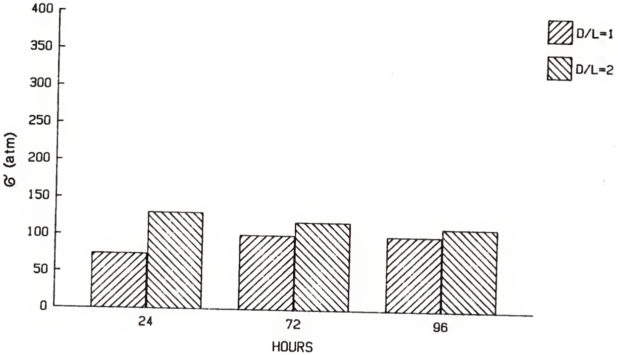

Fig. 25. Continued.
c) W/G = 3/4.

CHAPTER III

ANALYTICAL AND EXPERIMENTAL BACKGROUND

The spark induced shock waves are our major concern herein. However, before we study the shock wave, evolution, characteristics and propagation, it is necessary to review the known generating mechanisms of the shocks, in order to aid our complete understanding of the phenomenon.

Underwater Shock Wave Generating Mechanisms

Among the most important mechanisms for generating large pressure waves in fluids are 1) Electrostriction, 2) Dielectric breakdown, 3) Thermal Energy Deposition (thermoelastic process), 4) Vaporization, 5) Chemical Explosives and 6) Radiation. However, of these, radiation produced pressure waves have negligible strength in comparison with those produced by the other four interaction mechanisms. These mechanisms can be present either alone or in combination, depending on the intensity, pulse width or the power source and properties of the fluid [60]. Much work has been carried out on chemical-explosives-generated shock waves [67] and hence it will not be discussed here.

Dielectric breakdown is the most efficient mechanism in terms of generating very intense shock waves. The threshold voltage for inducing breakdown in pure liquids is high [61]. Below the breakdown threshold, molecular absorption of ohmic heating leading to vaporization and expansion characterizes the interaction [62-64]. This vaporization process and the correlated recoil momentum which acts in the liquid are only present if the vaporization threshold of the medium has been exceeded.

The thermoelastic process on the other hand is associated with the thermal expansion of a rapidly heated volume of the medium. Efficient thermoelastic sound generation requires short pulses with durations in the submicrosecond region. It is known that the pulse attributed to the thermoelastic effect is weaker than the pulse which is caused by vaporization [65].

The electrostriction effect as a stress generating interaction mechanism is important only for transparent media and for power intensities that imply an electric field strength of the order of 10^7 V/cm^2 [66].

It is of importance to consider some properties of the water medium as this plays a major role in not only generating stress waves but also in determining the generating mechanism. Table 2 defines the vaporization threshold of water which indicates the minimum amount of energy per unit volume that has to be absorbed by the liquid in order to induce vaporization. While the sound attenuation coefficient is important when considering the propagation of high frequency acoustic waves in liquids, the sound attenuation coefficient is proportional to the square of the sound frequency within a certain frequency range. And as long as no saturation of the absorption occurs, the absorption coefficient determines the absorbing volume of the liquid and hence the absorbed energy density.

Table 2. Water Properties.

vaporization threshold	2.6E9 (J/m^3)
sound velocity at N.T.P.	1.49E3 (m/sec)

Shock Waves

The effectiveness of the shock waves does not depend only on the pressure history but there are some other important factors which should also be considered in describing such effectiveness. These factors are 1) the pressure amplitude, 2) the shock impulse and energy flux density, 3) the shock duration, 4) loading rate and the rise time of the shock wave front. These factors constitute the characteristics of the shock waves.

The characteristics of the shock wave describe its propagation in a medium both in temporal and/or spatial form. It is important to point out that the effectiveness of the shock wave depends more on the impulse than on the pressure history. This is true, for example, in cases of structural damage for which the time of the deflection of the structure is much longer than the duration of the pressure in the incident wave. The impulse of a unit area of the shock wave front, up to a time t after its arrival, is given by the standard definition

$$I(t) = \int_0^t P(t)\ dt \tag{9}$$

Another significant measure of the shock wave effectiveness is the energy flux density E(t). For a shock wave in water at NTP, it is given by [69]

$$E(t) = 1/\rho_0\ C_0 \int_0^t P^2\ dt \tag{10}$$

where ρ_0 is the water density and C_0 is the speed of sound.

In addition to the above mentioned factors, there are other factors that may have an effect on the extracoporeal shock wave generated by the lithotriptor, namely: 1) the input voltage, 2) the inflation of the X-ray coupling balloons, 3) the electrode configuration and the spark gap size and 4) the carrier water condition. Some of the above mentioned factors are limited only to the ESWL technique used in crushing urinary stone.

In describing the pressure-density relation for shock waves, Tait's modified equation of state in water can be used. The advantage of that equation lies in expressing the compressibility coefficient as a direct function only of the pressure change, which is measurable. It can be written in the form

$$(P + B)/B = (\rho/\rho_0)^n \quad (11)$$

where

P is the pressure jump in atm.

ρ_0 is the density ahead of the shock front.

n is an adiabatic index of magnitude of 7.15 for water.

B is a weak function of the entropy, but may be assumed to have the constant value of 3000 atm. for relatively low pressures, i.e. up to thousands of atomspheres.

Using the equation of continuity, Skvortsov et al. [11] defined the expansion velocity of the spark channel (V_c) as a function of the shock front propagation velocity, V, and the coefficient of compressibility, c, as follows:

$$V_c = V\sqrt{(c-1)/c} \quad (12)$$

In addition, he expressed the particle velocity behind the shock front as

$$u = V_c\sqrt{(c - 1)/c} \quad (13)$$

Using the Euler equation, Skvortov et al. [11], after integration, found that the pressure in the channel is

$$P_c = P_f \{1 + c \ln [c/(c-1)]\}/2 \tag{14}$$

The relation between P_f and c is determined by the equation of the shock adiabat for water (which is approximately the same as for the isentropic case up to $8\text{x}10^4$ atm.)

$$P_f = 3050 (c^n - 1) \tag{15}$$

where

P_c is the pressure in the spark channel

P_f is the pressure in the shock front

Shock wave propagation has been the subject of many studies dating back to the work of Riemann in the 1870s. Three different theories for shock propagation in liquids have been established by Kirkwood-Bethe, Kirkwood-Brinkely and Penney-Dasgupta [67]. They are approximate developments from the basic equations of hydrodynamics, but the methods of the formation and approximations involved are quite different in the three cases. Unambiguous comparison of the various theories with each other and experimentally measured shock wave pressure is, unfortunately, not possible [67]. It was concluded that Penney's model is a more direct approach and inherently more satisfactory for the calculations of the initial formation and development of the shock wave.

Unfortunately, for the range of interest to us, Penney's method is not applicable to the propagation of focused shock waves. Penney and Dasgupta used an improved equation for state due to Bridgman and initial conditions based on Taylors [67] calculation for spherical detonation waves in TNT. Their analysis of explosion-induced shocks has been carried out to approximately 6 charge radii, at which point the shock wave pressure was found to have a nearly linear decay behind the front. The calculated values of the peak pressure P_m as a function of shock front radius R agreed closely with the formula

$$P_m(\text{psi}) = 103000\ a/R\ e^{2a/R} \tag{16}$$

over the range $a<R<6a$, where a is the charge radius. The range over which the equation is valid is so small that it is far away from the focal region of the pressure field. Therefore, it cannot be used in the present experiment near the discharge or near the second focus (F2) of the ellipsoid.

Rankine-Hugoniot equations, however, are universally valid for representing the conditions at the shock wave front. Their derivation depends on the assumption that a shock front can be regarded as a discontinuity in the fluid conditions behind and ahead of it. These relations are thus valid for the limit of negligible shock thickness. The Rankine-Hugoniot curves for water have been derived by a number of investigators [67] including Kirkwood and Montroll, Kirkwood and Richardson, Richardson, Arons and Halverson, Arons and Halverson and Doering and Burkhardt. In these treatments, systematic extrapolations of Bridgman's [67] PVT data for water were made. Probably the most comprehensive extrapolation of Bridgman's PVT data, however, was carried out by Snay and Rosenbaum [67].

When a mass element is traversed by a shock front, it suffers an almost discontinuous change in its thermodynamic state. The shock front propagates with a velocity, V, which is supersonic relative to the undisturbed medium; and a mass (or particle) velocity, u, is imparted to the material behind the shock front. The shock front velocity must be constant to satisfy the Chapman-Jouguet condition [68], that when the shock wave reaches the outer shell of the charge it continues to propagate in the outer undisturbed medium as a spherical blast wave. The conservation relations [69] for that process are

$$\rho_0(V-u_0) = \rho(V-u) \tag{17}$$

$$P - P_0 = \rho_0(V-u_0)(u-u_0) \tag{18}$$

$$E - E_0 = 1/2(P + P_0)(1/\rho_0 - 1/\rho) \tag{19}$$

where P_0, ρ_0, E_0 and P, ρ, E, denote pressure, density and specific internal energy ahead of and behind the shock front, respectively.

Dissipative Mechanisms and the Width of the Shock Front

In shock wave propagation, both viscosity and heat conduction are important only in the thin layer of the wave front whose thickness is of the order of the molecular mean free path, f.

In order to theoretically determine the structure and the thickness of the transition layer, one must take into account the viscosity and the thermal conductivity of the material in the transition zone. On the other hand, the viscosity and the heat conduction can be neglected if the dimensions of the system are much greater than the molecular mean free path (i.e., $L/f>>1$) and the velocity is smaller or close to the speed of sound ($V/C<1$). However, this condition is not satisfied in a shock front, the thickness of which is comparable to the mean free path. Hence, dissipative processes must appear within the shock front. These processes are responsible for the increase in entropy across a shock wave. The entropy increase indicates that there is dissipation of mechanical energy and that an irreversible conversion of mechanical energy into heat takes place in the shock front. The maximum entropy change occurs within the shock front. The existence of the entropy maximum is attributable to the fact that conductive heat transfer takes place from a high temperature region to a low temperature region. Therefore, the flow going into the region of the shock front is first heated by heat conduction, with an increase in entropy, and then cooled, with a decrease in entropy. The end state is the entropy will always be greater than the initial state.

Indeed, it is the viscous mechanism which converts a portion of the kinetic energy of the gas (or liquid) flowing into the discontinuity into heat; this conversion is equivalent to the transformation of the energy of ordered motion of gas molecules into the energy of random motion by the dissipation of molecular momentum. In this respect, heat conduction has an indirect effect on the conversion process, since it only participates in the transfer of the energy of random motion of the molecules from one point to another, but does not directly affect the ordered motion.

The shock front thickness can be defined in terms of the temperature, density, entropy or pressure jump across the shock front [70] as

$$L = f\ P_0/(P - P_0) \qquad (20)$$

Equation (20) shows that if the pressure jump in the wave is of the order of magnitude of the pressure ahead of the front, then, the front thickness will be approximately equal to the molecular mean free path. If the strength of the wave increases further, the same equation shows that the thickness becomes smaller than the molecular mean free path. Obviously, the thickness of an arbitrary strong shock wave cannot become larger than the molecular mean free path.

The front thickness is inversely proportional to the wave strength and the scale factor which is the molecular mean free path f. The thickness of the shock decays with time due to molecular diffusion and heat conduction. With the help of a fast rise time digital oscilloscope and a fast response transducer, the SW can be registered. Measuring the shock wave front (SWF) propagation velocity, the thickness of the shock can be determined easily without going into the complications of the theoretical speculations. Given the shock front thickness, the molecular mean free path can be determined based on equation (19).

It has been shown [70] that, without account of the viscosity, one cannot produce a continuous distribution of all thermodynamic quantities in the SWF; therefore it is necessary to estimate the dynamic viscosity in the shock wave front.

Since it is natural to assume that within the shock front the inertial forces are in equilibrium with the viscous forces, that is Re=1, where the Reynolds number $Re = \frac{\rho(LV)}{\mu}$ with ρ the density of the material, (V) the velocity and L the characteristic dimension and μ the dynamic viscosity.

Cavitation Phenomenon

Accompanying spherical shock waves in liquid is often the cavitation phenomenon. The simplest approximation to the true motion of a cavitation bubble is the one in which it is assumed that the motion of the surrounding water is entirely radial and that there is no migration (the noncompressive approximation). The equations of continuity and motion for the water can thus be simplified to be only in terms of the radial component. Although the basic hydrodynamical equations apply, exact solutions are difficult to obtain. An approximation to the kinetic energy for a cavitation bubble is [37]

$$K = 4\pi\ P\ R^3/3 \qquad (21)$$

where P is the pressure within the cavitation bubble and R is its radius. This relation thus furnishes an experimental method for determining, to a rather good approximation, the kinetic energy K associated with the radial flow of water in terms of the maximum radius Rmax of the bubble and the hydrostatic pressure P of the gas at the depth of the explosion.

Collapse Times of Gas Bubbles

The collapse time T_c of a spherical bubble with radius R is given by Rayleigh [34] as

$$T_c = 0.91468\ R \sqrt{\rho/P} \qquad (22)$$

This relation is valid since the shock wave has a very short pulse duration which is very much smaller than the collapse time of the bubble.

The Optimum Peak Pressure

Theoretical calculations of the pressures in water follow the incompressible approximation. While this assumption leads to a fairly accurate description of the main features of gas sphere motion, particularly of the maximum radius and the period of pulsation, it becomes an increasingly poor approximation as the bubble contracts to its minimum size with increasing velocities of the surrounding water and higher pressures. The latter part of the motion is often referred to as "bubble pulses" or secondary pressure waves which are emitted while the bubble is at or near its state of maximum contraction. The bubble pulse velocity is much smaller than that of the main blast wave.

Principles of Modelling of Urinary Test Concretions

After studying the evolution and the characteristics of both the shock waves and the accompanying cavitation phenomena, it was of importance to test the effect of such mechanisms on the materials. Unfortunately, using urinary stones did not yield any reliable information. That was due to the fact that urinary stones vary not only in composition but also in structure. Therefore, it was necessary to model such stones in terms of their compressive strength.

The selection of suitable materials to model urinary stones requires the selection of a cementitious material and the right relative quantity of water as well as monitoring the specimen strength as a function of its age.

Cementitious materials used thus far in modeling are Portland cement and gypsum plaster. Portland cement of the Type I, normal, and Type II, high early strength, commonly used in modeling, have been popular. But the attractiveness of using Portland cement is diminished considering that Portland cement requires 10 to 28 days to develop the required stable strength level. Severe shrinkage problems are often associated with the use of Portland cement which is an intolerable condition in super-scale modeling where thickness may be as small as a fraction of a centimeter. Another disadvantage of using Portland cement is that excessive strength variation associated with changes in specimen size has been found with Portland cement mortars [71]. Generally, increased tensile strength occurs with a reduction in specimen size.

The samples were made of Gypsum cement, which is widely used because of its more rapid hardening and drying and because it can be mixed uniformly. Gypsum cement originates from raw gypsum. The basic mineral is ground and calcined to produce a powder with uniform chemical and physical properties. The calcination process removes a portion of the chemically combined water in the following reaction:

$$\underset{\text{(gypsum)}}{CaSO_4 \cdot 2\ H_2O} + \text{heat} \dashrightarrow \underset{\text{(cement)}}{CaSO_4 \cdot 1/2\ H_2O} + 1\ 1/2\ H_2O$$

Since the reaction is reversible, adding water to the gypsum cement forms gypsum once again as follows:

$$CaSO_4 \cdot 1/2\ H_2O + 1\ 1/2\ H_2O \dashrightarrow CaSO_4 + 2\ H_2O + \text{heat}$$

Gypsum cement differs from gypsum plaster in the size and the shape of the crystals formed during the manufacturing process. The gypsum cement crystals require a smaller quantity of water to complete the reverse reaction, and thus result in a harder, stronger, and a denser finished product.

There are three main reasons for gypsum cement's superiority over Portland cement in super small scale modeling: 1) rapid curing time, 2) small particle size, and 3) low distortion. Gypsum cures rapidly and can actually be removed from its forms within 30 to 60 minutes after mixing. In fact, gypsum gains strength and stiffness by drying, and will become too brittle if allowed to air dry for a period of several days or longer.

Gypsum cement exhibits very low distortion upon curing. Unlike Portland cement mortars which contract, gypsum mortars expand. Maximum expansion for pure gypsum cement excluding aggregate is 0.080 percent.

No other cementitious material exhibits such a low distortion. With the addition of microaggregate, the expansion is even further minimized.

Gypsum cement is slightly soluble, amounting to about two grams per liter of water. This slight solubility is handy for cleanup after mixing and pouring. Furthermore, gypsum is also safe to work with. It is nontoxic, nonallergenic, odorless, and nondermatitic. It is noncorrosive, and noncombustible, and with a pH of 6.5 to 7.5, has a virtually neutral reaction.

Gypsum has been found to be compatible with a wide variety of chemicals, powders, and granular materials. However, gypsum crystals do not readily bond to aggregate larger than No. 10 mesh.

The water used in mixing should be low in contaminants. United States Gypsum recommends water between 70 F and 100 F, the temperature range in which gypsum has its maximum solubility.

Two types of gypsum cements used previously in modelling are Ultracal 30 and Ultracal 60, manufactured by United States Gypsum. The number is based on the approximate amount of time in minutes required for setting before the forms can be removed. Ultracal 30 has high surface hardness and compressive strength, and sets quickly. It is commonly used in industry and is the more readily available of the two.

Ultracal 60 is similar to Ultracal 30 except that its slightly higher consistency gives it less surface hardness and compressive strength. In addition, the longer set gives it less expansion.

Additives are available which retard the rate of setting. United States Gypsum recommends a sodate retarder. Retarders reduce the strength of the cement but may be necessary for use with intricate modelling. The addition of aggregate to the gypsum makes the mix similar to concrete. This is especially evident in the effects on tensile strength. The ratio of compressive strength to tensile strength for pure gypsum is much higher than for concrete. The addition of aggregate lowers the tensile strength.

The effect of varying the water/gypsum cement ratio and the aggregate/gypsum ratio has been studied by Sabnis and White [71]. In that study, it was shown that the addition of both water and aggregate lowers the compressive strength. It should also be remembered that water in excess of the amount required to complete the reaction with the plaster will be removed by the drying process, resulting in air voids.

Gypsum mortar, consisting of gypsum, sand and water have been used also in modelling. But they possess a potential problem because they develop strength rapidly even during prolonged testing. In addition to the age, the amount of moisture present in different size specimens is by far the most important parameter in observed size effects. This problem can be alleviated by sealing the moisture in the mixing at the desired strength level. Sikaseal, Thoroclear, and ordinary shellac have been found to be effective sealants. Sabis and White [71] report that unsealed specimens gave an increase in strength of about 50 percent as specimen diameter decreased from 8 cm to 1 cm, while surface sealed cylinders gave no measurable size effect. Their findings indicate the 1 cm deep beams were only ten percent stronger than 7.5 cm beams in rupture, and therefore the size effect could be considered insignificant. An infinite number of variations in the mix could be achieved by changing the water/cement ratio, the water/aggregate ratio, the type and gradation of aggregate, and the type of cementing agent.

It is now important to summarize the factors which play a major role in cement-gain/loss of strength. The primary factor that governs the strength of such a brittle material is the capillary porosity. However, this is not an easy quantity to measure or predict, therefore the capillary porosity of a properly compacted cement is usually determined by the water-cement ratio (w/c) at any degree of hydration. Hence, the lower that ratio (full compaction) the higher the strength and vice versa. That is simply because of a better mechanical bond. The limitation, however, of the w/c lowness is cement that is not properly compacted since it contains large voids which contribute to its porosity. The rate of strength gain depends on the initial w/c ratio, where low w/c mixes gain strength more rapidly than higher w/c ratio mixes.

The time and the temperature together play a major role on the hydration rate and hence control largely the gain in strength. It is known that cement that hydrates more slowly tends to develop higher ultimate strength.

Fineness of the cement also has an effect on the rate of hydration, whereas the latter increases with increasing fineness and leads to higher rate of strength gain but very fine grinding should be avoided because the interstitial water may lead to regions of high w/c ratio.

It is worth noting here that cracks tend to be more stable in compression than in tension. In addition, it has been found by many investigators that the tensile failures that are produced by compression loads occur at higher strains than those failures due to direct tensile stresses.

The tensile strength is higher for moist-cured cement than it is for air cured. On the other hand, incomplete compaction and air entrainment affect the compressive strength more than they do the tensile strength.

CHAPTER IV

EXPERIMENTAL RESULTS

The underwater spark explosion induced at the first focus (F1) of a semi-ellipsoidal reflector is a complex phenomenon. It causes more than a shock wave to be created and more than one cavitation bubble to be formed. When the short duration spark is discharged at F1, an initial spherical shock wave is produced. Part of this direct shock wave (DSW) propagates along the Z axis of the reflector shown in Fig. 1. The remaining portion of this shock (DSW) is reflected back upon reaching the reflector wall forming a converging shock termed the reflected shock (RSW). This RSW converges to almost a point as it approaches the second focus (F2) of the ellipsoidal reflector.

Cavitation bubble collapse generally radiates a secondary shock wave (SSW). Specifically speaking, the cavitation bubble formed at F1 of the reflector emits a SSW when the bubble collapses. This SSW is decomposed into a direct and a reflected shock according to the reflector property.

Cavitation has been found to follow the evolution of the shock wave both at the first focus (F1) and at the second focus (F2) of the reflector. The former is due to superheating of the water as a result of the high temperature generated by the spark. The latter however, is due to such a drop in the water pressure that the vapor pressure has been reached and cavitation is produced.

Fast pressure transducers provide an excellent tool for the study of the individual characteristics of the shock waves and cavitation as well as contribute to the understanding of the fracture mechanisms for urinary stones. The pressure history of the detailed spark induced explosion phenomena recorded at F2 is shown in Fig. 26. In that figure, we can see that there are six different pulses within a period of time of about 1.2 milliseconds. The first pulse shown on the trace marks the time of the applied voltage which is basically our time t = 0. Not long after this, a spherical shock wave forms and propagates directly upstream from the origin (F1) along the Z axis shown in Fig. 1. This direct shock wave (DSW) is detected after about 150 microseconds and labelled 2. The reflected or focused shock wave (RSW) first registers at F2 after about 180 microseconds and is labelled 3, as shown in Fig. 26. In other words, this happened 30 microseconds after the arrival of the direct shock (DSW). About 760 microseconds after the voltage pulse another pulse was detected and is labelled 4. This pulse is a secondary shock wave emitted from the cavitation bubble formed at F2 after it has abruptly reversed its phase from full contraction to expansion. This

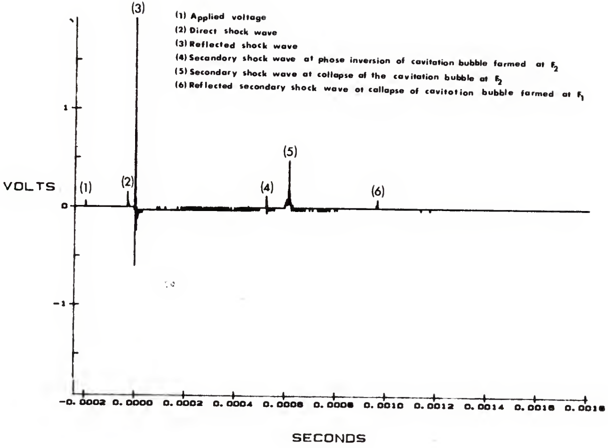

Fig 26. Spark induced phenomena at F2 in ESWL. The voltage represents the direct signal from the lithium niobate transducer.

bubble collapses after another 60 microseconds and is labelled 5 on the trace. Thus, the collapse of the cavitation bubble formed at F2 occurs about 830 microseconds after the applied voltage. Last on the trace we find the pulse labelled 6. This pulse denotes the reflected component of the secondary shock wave produced by the collapse of the cavitation formed at the first focus (F1) of the ellipsoid. That pulse has registered after the applied voltage by about 1.2 milliseconds. It should be mentioned that the direct component of that pulse has fully dissipated during its direct propagation to F2.

Tracing the above phenomena at different standoff distances from F2 along the Z axis, we found, as clearly shown in Fig. 27, that at 5 mm above the nominal geometrical objective focus (F2), the bubble does not reverse its contraction phase as it collapses at the end. At further distances away from this standoff distance, the bubble seemed to reverse its phase. Therefore, we can conclude that this cavitation bubble forms at 5 mm above F2, and this position will be referred to as the dynamic focus (Fd).

Cavitation formed at F1 is of secondary interest as a fracture mechanism for urinary concretions since the amplitude of its reflected shock, the only component reaching F2, has almost dissipated during its propagation to F2. Cavitation formed at F2 is, however, considered a major fracture mechanism for urinary concretions. It can be seen in

Fig. 26 that the magnitude of the pressure produced by the cavitation bubble at F2 is about 20% of the magnitude of the pressure of focused shock (RSW).

Cavitation generally does not directly break up stones. It may cause chipping off any exposed surface (43) and eventually cause fracture of the material. Thus, it can be concluded that the focused shock wave (RSW) is the major direct fracture mechanism for urinary calculi. This conclusion is in agreement with a study on the effect of the above mechanisms on simulated urinary calculi to be discussed below.

It becomes important to study the focused shock wave more thoroughly and the effect of some factors, pertaining to the Lithotriptor, on the RSW intensity and its focusing quality. These factors include the inflation of the para-ellipsoid X-ray coupling balloons, the electrode spark gap size, the condition of the coupling water medium and the input voltage.

Analysis of the Characteristics of the ESWL

In examining the rate at which the electrode spark gap wears out, we found as shown in Fig. 28, that the wearout behaves logarithmically for increasing number of shocks and follows the equation

$$S_g = -1.7 + 0.61 \log_{10} N \quad . \; . \; . \quad N \geq 32 \qquad (23)$$

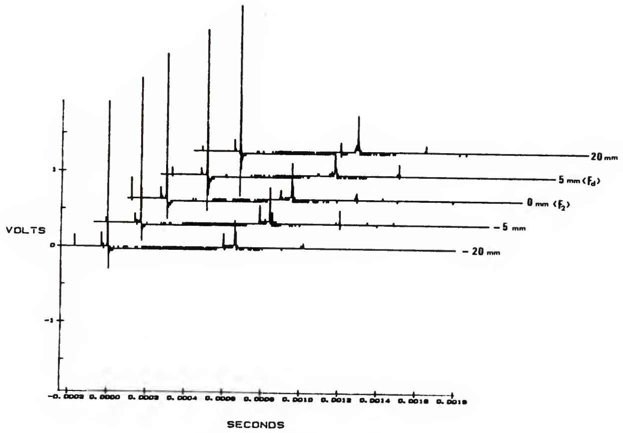

Fig. 27. Spark induced phenomena at different standoff distances along the reflector Z axis in ESWL.

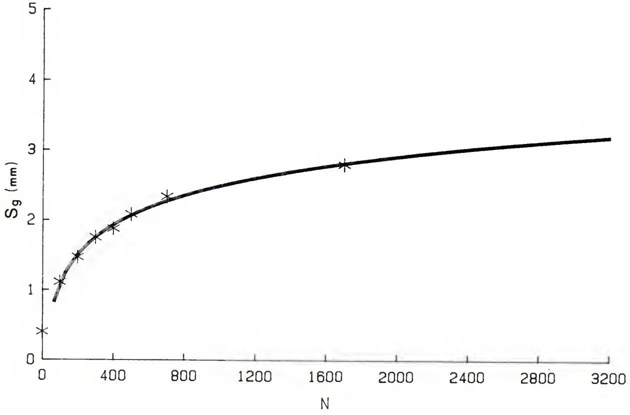

Fig. 28. The wearout of the electrode spark gap (Sg) for increasing number of triggered shocks (N).

where S_g is the electrode spark gap in mm and N is the number of triggered shocks.

The electrode spark gap size has proven to be a factor that can affect the shock pressure field. In other words, the rapid decay of the pressure amplitude for increasing or decreasing distance from the objective focal point has proven to depend on the electrode spark separation or gap. It is found that the pressure decays faster in space along the X axis for the large gap than at the small gap as shown in Fig. 29a, while the pressure falls off somewhat faster along the Y axis with the small gap as can be seen in Fig. 29b. The change in the pressure pattern due to the change in the gap size along the X and Y axes is however very slight compared to that along the Z axis (Fig. 24c). It can clearly be seen in that figure that the pressure field does not converge sharply to a point but the focus is a zone or a region of a height termed the depth of focus. It is obvious that the depth of focus at the small gap is greater than that at the large gap; namely, 10 mm with the small gap compared to 5 mm with the large gap. Farther along the Z axis, above F2, the pressure produced by the large gap electrode decays faster than that produced by the small gap electrode. As the RSW pressure field approaches F2 however, the buildup of the pressure produced by the large gap electrode is slower than that produced by the smaller gap electrode. It is also found that the larger the electrode spark gap the lower the pressure magnitude. The

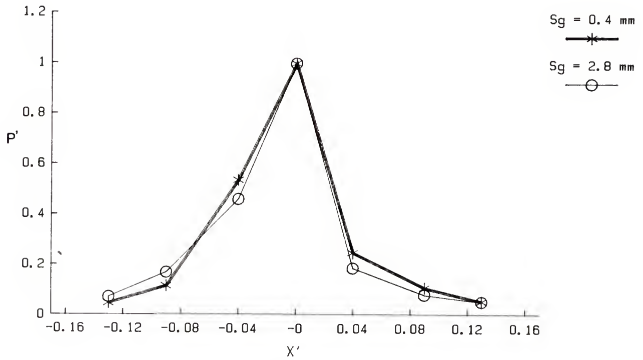

Fig. 29. The effect of the electrode spark gap size on the pressure distribution along (a) X axis through F2 where P' is the pressure normalized to the maximum pressure of both gaps while X' is the distance along the X axis relative to the distance between the foci of the ellipsoid which is 23 cm (i.e., F1-F2).

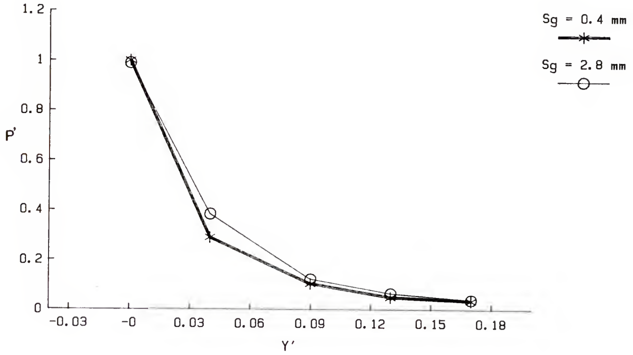

Fig. 29. Continued.
(b) Along Y axis up to F2 where Y' is the distance along the Y axis relative to the distance between the foci of the ellipsoid. Mirror symmetry is assumed.

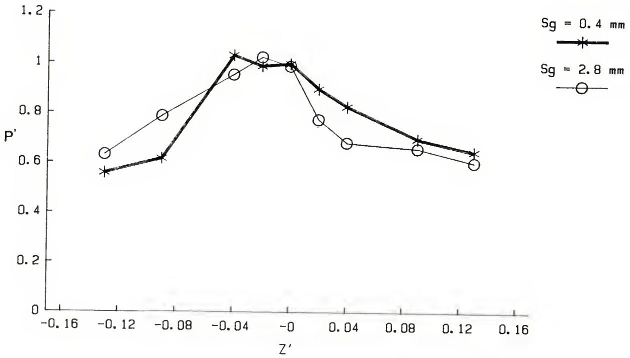

Fig. 29. Continued.
(c) Along Z axis through F2 where Z' is the distance along the Z axis relative to the distance between the foci of the ellipsoid.

decrease however, as can be seen in Fig. 29c, is about 1%. That observation is in contradiction with Chaussy et al. [3] but is in full agreement with the basic principles which suggest that the smaller the spark channel the higher the energy density carried by the coupling fluid and delivered to the shock wave.

It is important to point out that it is not necessarily true that the geometric object focus carries the highest intensity. In fact, as shown in Fig. 29c, the dynamic focus (Fd), where the maximum pressure occurs, is below the geometric focus (at Indianapolis site). This suggests that the shock wave self-diffraction might be the reason for the shifting of the objective focus. Self-diffraction is believed to be caused by either some imperfection in the ellipsoidal reflector, or the electrode spark channel (gap) is not exactly positioned at the geometrical first focus of the reflector. This means that the position of the dynamic objective focus differs from one reflector to another and consequently from one Lithotriptor to another. This fact has proven to be true as shown in Fig. 30. These measurements were obtained by us at different locations. Furthermore, the dynamic objective focus was found to shift closer toward the geometric focus when a larger spark gap electrode is used.

Conceptually, it is interesting to think of three definitions: 1) the geometric objective focus, 2) the dynamic objective focus (i.e. the region of maximum shock intensity) and 3) the region of maximum pulverization or fracture. The

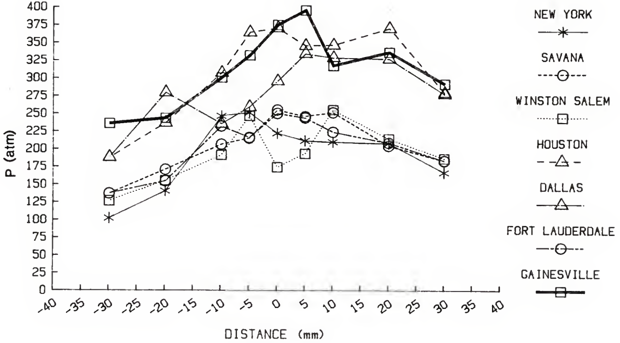

Fig. 30. Spatial distribution of the reflected shock pressure along the Z axis of the reflector for seven different lithotripters.

location of the latter is a function of the properties of the material being shock tested and its position along the shock path. This subject will be discussed later.

Investigating the effect of the inflation of the para-ellipsoid X-ray coupling balloons on the intensity of the RSW, we found that there is not a considerable decrease in the pressure magnitude. However, when the balloons are so inflated that they overlap on the reflector mouth, they will interfere with the RSW pressure field. Such interference not only attenuates the shock pressure but can fully dissipate it. As can be seen in Figs. 31a,b, the inflated balloons round off the sharp focused pressure and lower the pressure magnitude a little.

Keeping the other variables constant while varying the discharge voltage to study its influence on the effectiveness of the RSW in terms of the pressure magnitude, the shock impulse, the energy flux density, the duration and rise time, we found, as can be seen in Figs. 32a,b, that the governing relationship is linear; that is, the higher the input voltage, the higher the RSW pressure, impulse and energy flux density. Conversely, the higher the input voltage, the shorter the shock duration and the faster its rise time.

The coupling water medium condition in terms of the air content and the temperature may also affect the intensity of the RSW pressure magnitude. It is found that the longer the degassed water is exposed to the environment, the lower the

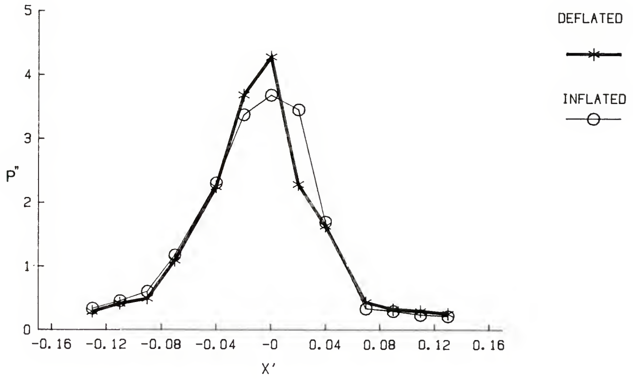

Fig. 31. The effect of the inflation of the para-ellipsoid ballons on the pressure distribution (a) along X axis where X' is the distance along the X axis normalized to the distance between the reflector foci and P" is the pressure along the x axis normalized to that at a reference position.

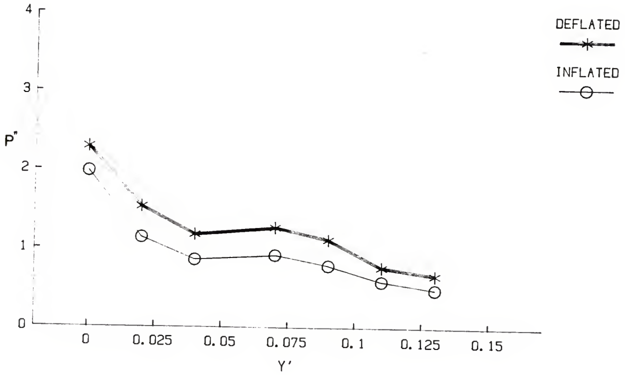

Fig. 31. Continued.
(b) Along Y axis up to F2 where Y' is the distance along the Y axis normalized to the distance between the reflector foci. Mirror symmetry is assumed.

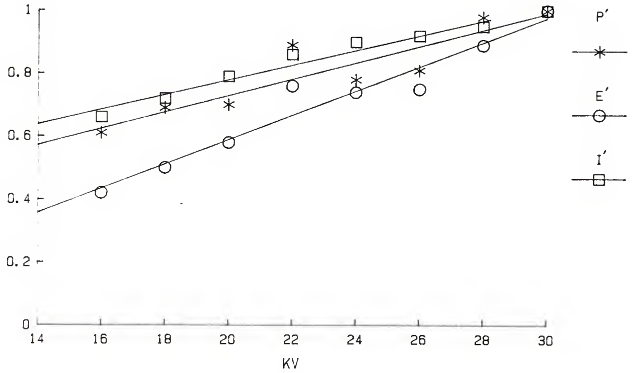

Fig. 32. The effect of the input voltage (a) on the pressure, energy, and impulse patterns at F2 where E' is the energy of the focused pulse normalized to the maximum energy present, while I' is the impulse normalized to the maximum impulse. P' is the pressure normalized to the maximum pressure.

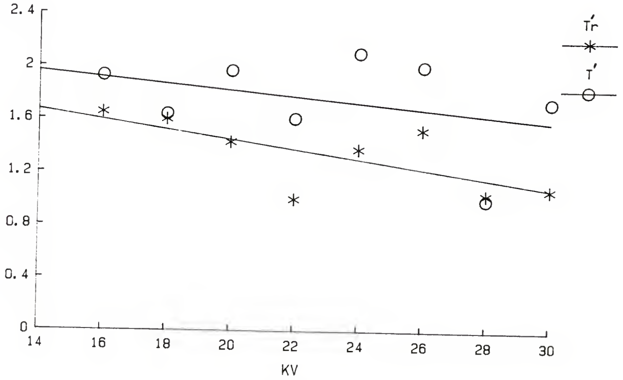

Fig. 32. Continued.
(b) On the rise time and duration of the focused shock at F2. Tr' is the rise time normalized to the fastest rise time, while T' is the duration normalized to the shortest duration occurred.

pressure magnitude. This is due to the fact that the water absorbs air and gases from the surroundings and this helps induce pseudocavitation which can absorb a considerable amount of the energy release, including the energy contained in the shock wave.

It should be mentioned that the temperature of the water has no effect on the shock waves both for the DSW and the RSW; however, it might have an effect on the secondary shock waves generated due to cavitation.

After studying the effect of the ESWL characteristics on the RSW intensity we can start examining the shock wave characteristics and their generating mechanism.

Shock Generating Mechanisms

In studying the generating mechanism of the shock waves, we found that dielectric breakdown and vaporization were the dominating mechanisms. That fact was proven based on the energy density in the spark channel. It was found that the energy density in a spark channel of 0.4 mm wide (new electrode) is 1.14E13 J/m^3 at 20 KV and that for 2.8 mm spark channel wide (old electrode) is 35E9 J/m^3. Both are well above the vaporization threshold as well as above the dielectric breakdown threshold, which is 5E11 W/cm^2. The energy density, even at lower voltages, is still well above the vaporization threshold. This estimate is based on the assumption that the spark gap is a spherical shape. It should be mentioned that this threshold is considerably lowered by the presence of impurities [72].

It is important to point out that the spark-induced dielectric breakdown is the major direct generating mechanism of both the DSW and the RSW. On the other hand vaporization is the indirect generating mechanism of the secondary shock wave produced by the cavitation bubbles formed at both F1 and F2.

The short duration spark generated at F1 gives rise to other physical phenomena. After the spark is fully discharged, visible light has been observed. That emission of light termed electroluminescence arises from a gas discharge in a bubble formed at the electrode spark channel [73]. That luminescence also is evidence that some of the electrons in the water reach energies of 2 eV to 3 eV or higher which is sufficient for ionization [73].

After examining the shock generating mechanism, we find that our immediate research needs are to describe the generated shock waves in terms of the temporal and spatial distribution of their properties.

Analysis of Direct Shock Wave (DSW)

As a result of releasing energy within a short period of time at F1, an initial spherical shock wave is created. It then propagates directly upsteam along the reflector Z axis shown in Fig. 1. While still confined within the ellipsoidal reflector, the shock reaches a radius of 2.5 cm within the reflector. By that time, which is 15 microseconds, the lower part of the shock makes the first contact with the reflector boundary, specifically the reflector dead end. The spherical shock then seems to decompose into two separate spherical shocks. On the other hand, the upper part of the initial spherical shock goes on propagating directly towards the second focus of the reflector. It results from the rapid release of the electrical energy and follows a direct path in propagation from its origin F1 to F2. This part of the shock is termed the direct shock wave (DSW). The DSW reaches F2 150 microseconds after the applied voltage, as shown in Fig. 26. Further details of the interaction of the initial shock with the reflector boundary are not of our concern in this part. It will, however, be discussed later when we describe the reflected shock wave (RSW).

By analyzing the direct shock wave (DSW) along the reflector Z axis, it is estimated that the rise and the decay time at the second focus of the ellipsoidal reflector (F2) were about 400 nsec and 600 nsec, respectively, based on 10% to 90% of the corresponding total front and tail duration. The shock wave duration, however, is about 800 nsec, based on 50% of the total width. The pressure magnitude measures about 12 atm, while the energy flux density and the shock impulse are about 0.6 Pa•m and 1 Pa•sec, respectively.

The shock pressure at F2 is characterized in the time domain by an approximately linear rise to its maximum amplitude shown in Fig 33. It follows the equation

$$P = P_m \ (0.157 + 1.7 \ t) \ . \tag{24}$$

Similarly, the shock decays to the ambient condition linearly as shown in Fig. 34 and follows the equation

$$P = P_m \ (1.03 - 1.1 \ t) \ . \tag{25}$$

Some variation in the pressure magnitude was noticed from one shock to another. It is believed that such fluctuation in the pressure is due to the variation of the velocity of the electrode spark channel expansion over which there is no control.

In investigating how the impulse and the energy flux density behave in time at F2, it can be inferred from Fig. 35 that the mass flow momentum in the shock front increases over the mass flow momentum out of the front in time until the shock dies out. That is to say, the momentum imparted to the water by the shock front increases over the shock duration. Similarly, the energy flux density after the shock arrival increases over the duration of the shock.

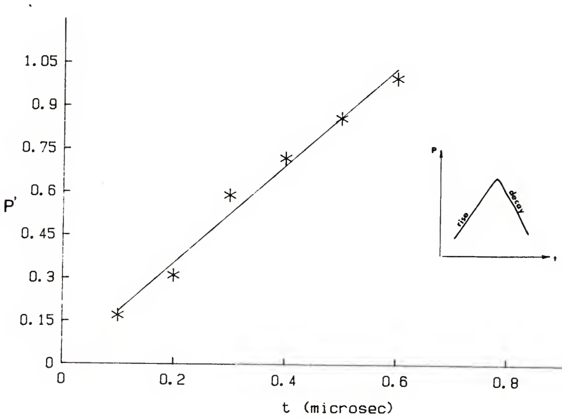

Fig. 33. Temporal distribution of the direct shock (DSW) pressure rise at F2. P' is the direct shock pressure normalized to the maximum magnitude.

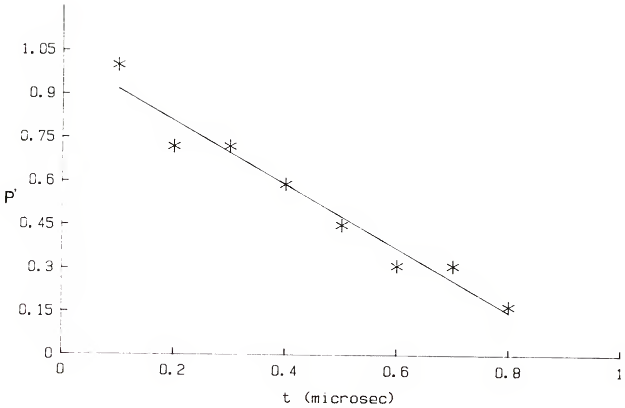

Fig. 34. Temporal distribution of the direct shock pressure decay at F2. P' is the pressure normalized to the maximum pressure magnitude.

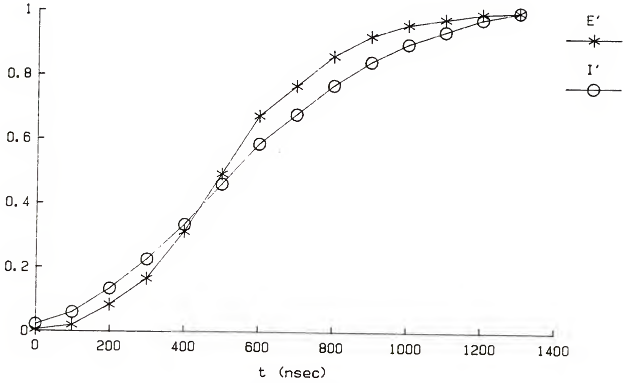

Fig. 35. Temporal distribution of the direct shock impulse and energy flux density at F2. E' is the energy flux density normalized to the maximum value and I' is the shock impulse normalized to its maximum value.

In other words, the energy transport, as a result of the shock passing through a surface area, increases with increasing time over its entire duration until the shock has totally died out.

The decay of the pressure amplitude in space along its propagation direction satisfies the 1/R law and hence it satisfies the already developed theory [67] based on explosive-generated spherical waves. The pressure along that direction is characterized by a linear decay, as shown in Fig. 36, as it follows the following equation:

$$P = [-0.1685 + 27.9(1/R)]\ P_f\ , \tag{26}$$

where P is the pressure magnitude of the direct shock and P_f is the maximum pressure occurring at the focal region and R is the distance from the electrode gap along the Z axis. The energy flux density, however, is characterized by a decay that follows the equation

$$E = (883.89\ (1/R)^{2.15})\ E_f\ , \tag{27}$$

where E is the energy flux density of the direct shock, E_f is the maximum value occurring at the focal region and R is the radius of the direct shock wave that originates at the first focus of the ellipsoid. The impulse, however, has a linear decay, as shown in Fig. 37, and follows the equation

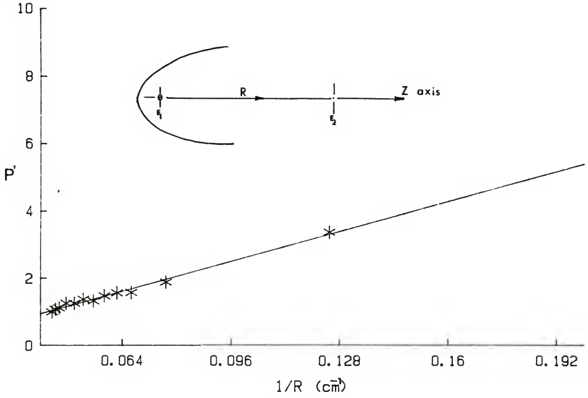

Fig. 36. Spatial distribution of the direct shock pressure along the reflector Z axis. P' is the pressure normalized to its maximum magnitude at F2.

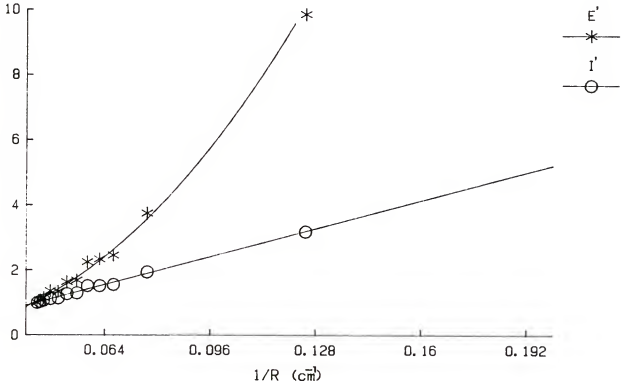

Fig. 37. Spatial distribution of the direct shock impulse and energy flux density along the reflector Z axis.

$$I = [-0.161 + 26.89\ (1/R)]\ I_f\ , \tag{28}$$

where I is the impulse of the direct shock (DSW) and I_f is the maximum impulse occurring at the focal region.

As can be seen in Fig. 38, the rise time and the duration of the DSW have been correlated to one another along the Z axis.

It was found that the shock front propagation velocity is about 1667 m/sec at F2. The shock front propagates with the same velocity at different standoff distances along the Z axis, before the reflected shock has a chance to develop. The only explanation for this phenomenon is that the energy transfer continues and hence the energy stored in the shock as a kinetic energy increases. This finding is in agreement with Skvortsov [11], who suggested that the transfer of the energy by small perturbations and weak shock waves, which are produced at the surface of the channel by mixing of the hot internal gas layers in the channel and the cold outer layers, are the cause for keeping the shock velocity constant while propagating.

Given the shock propagation velocity and measurements of the pressure jump at the second focus, equations (17) and (18) can then be solved for estimating the density behind the shock front. This is found to be about 1000.5 kg/m^3 at the second focus. It is obvious that the density change is so small that it can be considered negligible since the compressibility coefficient is estimated to be about 1.0005.

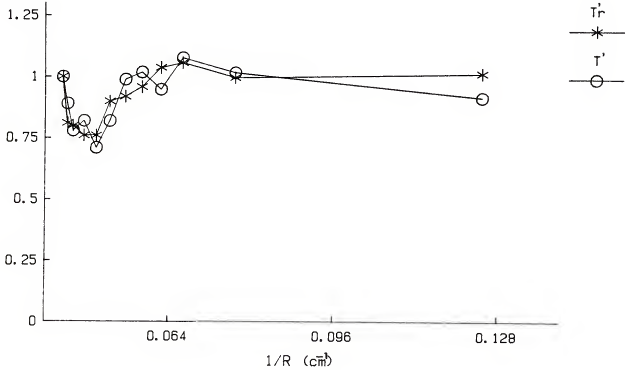

Fig. 38. Spatial distribution of the direct shock duration and rise time along the reflector Z axis. Tr' is the rise time normalized to the fastest rise time and T' is the duration normalized to the shortest duration.

On the other hand, in measuring the shock front propagation velocity, the particle velocity behind the shock front was estimated to be 1 m/sec. In addition, the shock wave front thickness is estimated to be 670 microns based on the average rise time of 400 nsec. Moreover, the dynamic viscosity in the shock front has been estimated to be 834 Pa·sec. It is obvious that the viscosity rose drastically compared to that of the water at normal conditions and 30 C. That estimation is based on the assumption that the inertial force is in equilibrium with the viscous force (i.e., $Re \cong 1$, where Re is the Reynolds number which is the ratio of the inertial forces to the viscous forces). This is clear evidence that viscosity must be considered as a dissipative mechanism which plays an important role in consuming some of the kinetic energy stored in the shock front.

The expansion velocity of the spark channel could be estimated by using equation (12), if the pressure inside the spark channel is measured. The measurement of the latter would be very difficult to obtain in view of the probable damage to the instrumentation.

Characteristics of Focused Shock Wave

After the initial spherical shock wave forms at the first focus (F1) of the ellipsoidal reflector, part of it eventually comes in contact with the reflector boundary. Every contact point becomes a generating point for a new spherical shock wave. These reflected shock waves are focused toward the second focus F2 of the ellipsoidal reflector. While propagating, the reflected shock waves interact with each other to form a cone-like field. This shock field, which is outlined by the shock interaction points, called "Mach Points," can be defined as the reflected (focused) shock wave (RSW). As the RSW approaches F2, it ultimately converges to a point at the second focus of the reflector.

Analyzing the RSW properties in the time domain, we found that the pressure apparently rises linearly to its maximum magnitude of 400 atm at Fd (the dynamic objective second focus, 5 mm above F2) in about 450 nsec, as shown in Fig. 39. The rising pressure follows the equation

$$P = (-.016 + 1.76\ t)\ P_m\ . \tag{29}$$

Similarly, the pressure falls off linearly to the ambient condition in about 575 nsec, as shown in Fig. 50. The following equation was found to fit the pressure decay:

$$P = (1.66 - 1.29\ t)\ P_m\ . \tag{30}$$

The duration of the RSW (time the shock takes to rise and fall back to the ambient conditions) was found to be 550 nsec at Fd, based on 50% of the total width.

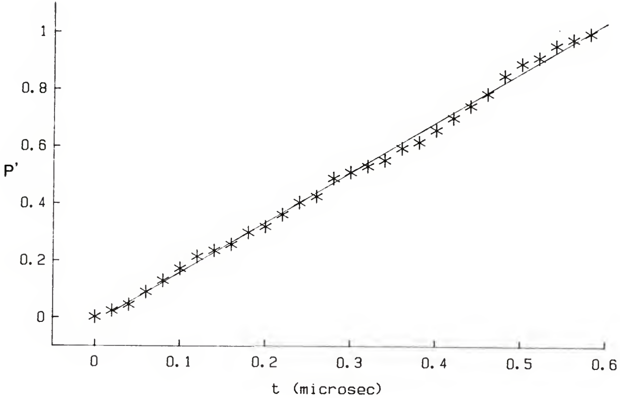

Fig. 39. Temporal distribution of the reflected shock (RSW) pressure rise at F2. P' is the pressure normalized to the maximum magnitude.

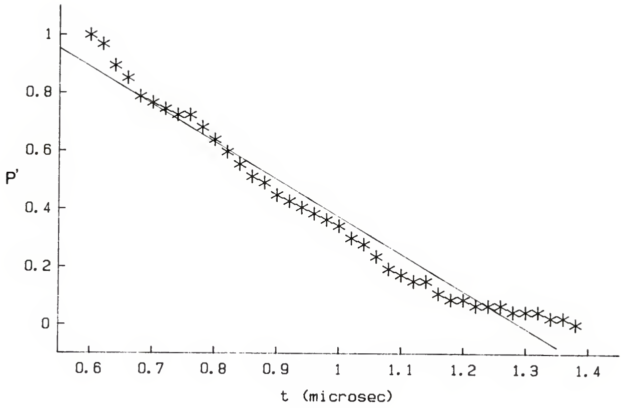

Fig. 40. Temporal distribution of the reflected shock pressure decay at F2. P' is the pressure normalized to its maximum magnitude.

The shock impulse, the momentum imparted to the water by the shock front passage measured at Fd, was about 28.4 Pa•sec. The energy flux density behind the shock front at Fd, however, is 115 Pa.meter. The temporal distribution of the impulse and the energy flux density over the shock duration are shown in Fig. 41. They increase drastically with increasing time. This means that both the front and back of the shock contribute to the shock intensity.

Analyzing the reflected shock wave (RSW) in the frequency domain, we found that the maximum power of the shock occurs at almost zero frequency level. This finding explains why the ESW is an effective fracture mechanism for urinary stones, particularly since high frequency signals are strongly attenuated in liquids [74].

The spatial distributions of the RSW characteristics have been examined. In the analysis, we found that the RSW pressure field in the X-Y plane at F2 is quite concentrated, as shown in Fig. 42. In Fig. 43, we show a contour map of this pressure distribution in the Y-Z plane at F2. It is clear that away from the second focal region of the reflector the pressure falls off very rapidly from its maximum magnitude.

Along the Z axis, however, we find that the highest pressure magnitude occurs at a position different from the geometrical focus (F2). This is shown in Fig. 44. The position of maximum dynamic focus is denoted as (Fd) and is located at about 5 mm from the geometric focus (F2) here at

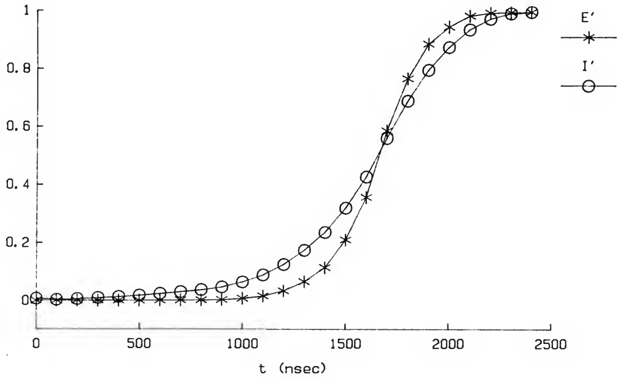

Fig. 41. Temporal distribution of the reflected shock impulse and energy flux density at F2. I' is the impulse normalized to its maximum value and E' is the energy flux density normalized to its maximum magnitude.

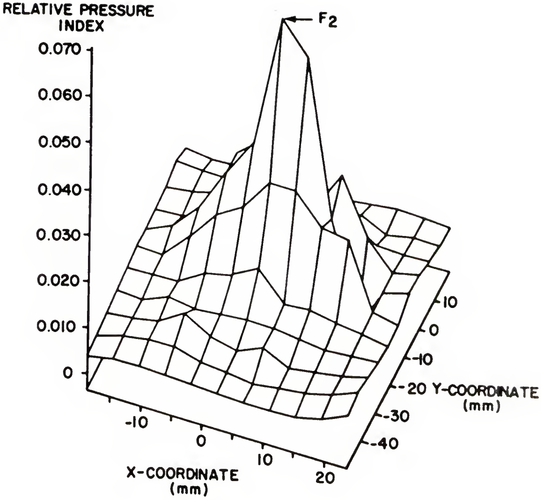

Fig. 42. 3-D representation of the reflected shock pressure in X-Y plane at F2.

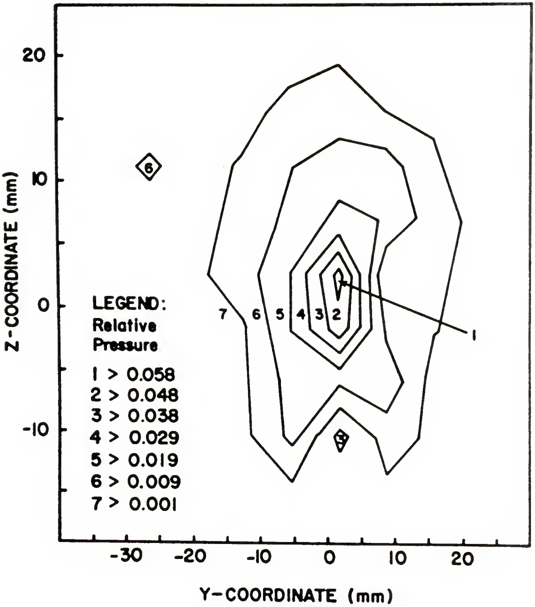

Fig. 43. Contour representation of the RSW pressure along Y-Z plane.

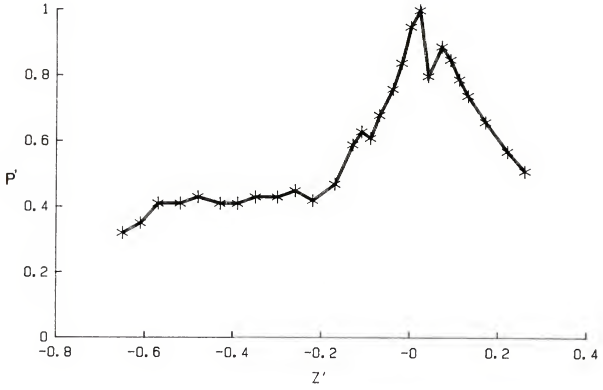

Fig. 44. Spatial distribution of the reflected shock pressure along the reflector Z axis. Z' is the distance along the Z axis measured from F_2 and normalized to the distance between the reflector foci and P' is the pressure normalized to the maximum magnitude occurred.

J. Hillis Miller Health Center, Gainesville. It should be mentioned that the pressure increase at the dynamic focus is about 5% over that at the geometric focus.

The shock pressure distribution along the Z axis can be fitted to exponential curves as shown in Fig. 45. In that figure we can see that the RSW rises to its maximum pressure magnitude and decays along the Z axis following the equation

$$P = P_m \left[\begin{matrix} 0.9e^{3.6Z'} \\ e^{-2.6Z'} \end{matrix}\right] \qquad (31)$$

where the upper term is valid in $-.17 > Z' > 0.0$ and the lower term is valid within $0.02 > Z' > 0.3$.

Over a longer range of the reflector Z axis, the spatial distribution of the RSW characteristics are no longer exponential and given by the distribution shown in Fig. 46. The decay of the pressure along the Z axis can be divided into three parts. In the first part where the pressure drops sharply from its maximum magnitude, we believe that once past the dynamic focus the field diverges and consequently the pressure falls off. In addition, an expanding wave forms and consequently a tensile stress in the water starts to be generated. When the tensile stress is superimposed over the compressive stress (pressure), this will result in lowering of the magnitude of the compressive stress drastically. The second part begins when the pressure rises in magnitude again. At this point, it seems that

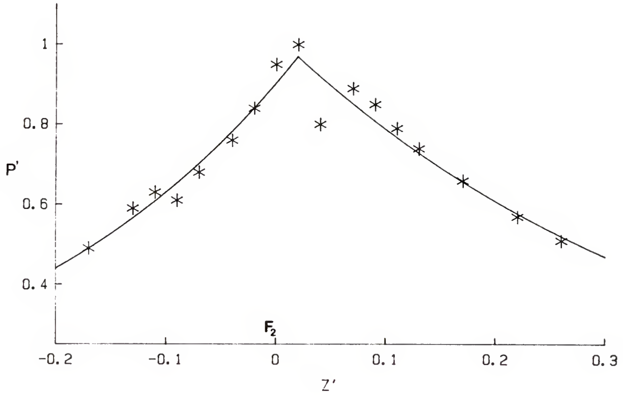

Fig. 45. Convergence and divergence of the reflected shock pressure field along the reflector Z axis.

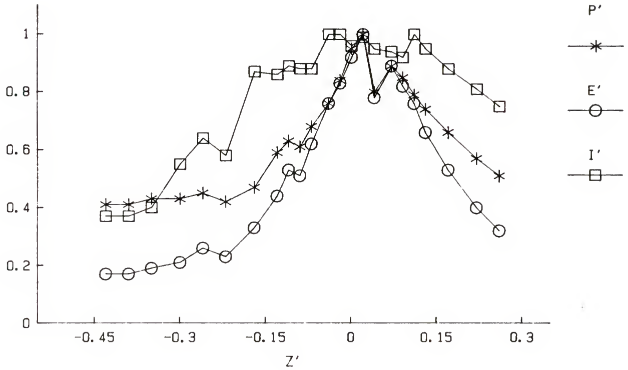

Fig. 46. Spatial distribution of the reflected shock pressure, impulse and energy flux density along the reflector Z axis.

the tensile effect starts to fade out until it becomes negligible. The third part occurs where the pressure is back on its exponentially decaying pattern.

It is also evident, as shown in Fig. 46, that the energy flux density stored behind the shock front rises more rapidly than does the pressure. The highest magnitude of the shock impulse is clearly shown to be located in the focal region.

The RSW propagation velocity (the difference between the reflected and direct shock path divided by the time difference between their arrival to the second focus), as can be seen in Fig. 47, is rising linearly along the Z axis. The shock wave propagates supersonically with a velocity of about 1770 m/sec or Mach 1.18 at F2. The increase of the shock front velocity for increasing distance from F1 is a result of the superposition of the shock waves along the propagation direction. In other words, it is due to the convergence of the shock waves along the propagation direction.

Examining the propagation of the focused shock (RSW) with respect to the direct shock (DSW) along the Z axis of the reflector, we found that the dominating correlation of pressure is exponential, as shown in Fig. 48, and fitted by following the equation

$$\tilde{P} = 7.35e^{3.21Z'} \quad . \qquad (32)$$

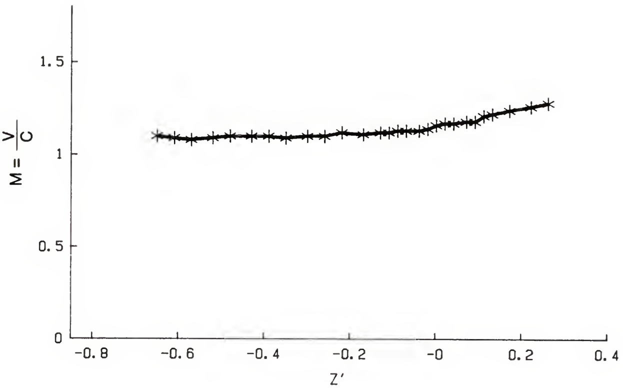

Fig. 47. Spatial distribution of the reflected shock propagation velocity along the reflector Z axis. M is the Mach number and Z' is the distance along the Z axis normalized to that between the reflector foci.

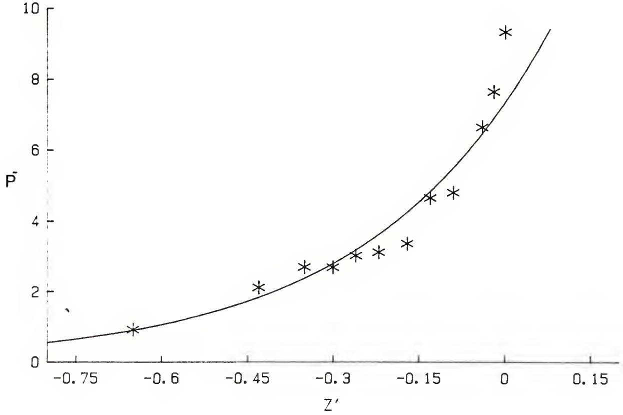

Fig. 48. Dissipation of the reflected shock pressure with respect to that of the direct shock along the Z axis. $\tilde{P}$ is the relative pressure index.

The distribution of the shock wave duration and its rise time (time the shock takes to rise from ambient to maximum pressure) along the Z axis can be seen in Fig. 49. In the figure it is clear that the duration is shortest at the dynamic focal point and the shock rise time seems to be about the same order of magnitude, which is about 450 nsec near the focus.

The shock front thickness at Fd, and the dynamic viscosity, have been estimated to be 800 microns and 1453 Pa.sec, respectively, based on a rise time of 450 nsec.

The compressibility coefficient has a value of about 1.018, based on the assumption that the inertial force is in equilibrium with the viscous force. In addition, the density behind the shock front was estimated to be about 1018 kg/m^3. From the conditions ahead of the shock front, the particle velocity behind the shock front has been estimated by using the Rankine-Hugoniot equation (18) to be 23.4 m/sec.

EHL Reflected Shock Wave Analysis

We examined the focused or reflected shock wave (RSW) produced by the Electrohydraulic Lithotriptor (EHL) within the test chamber shown in Fig. 12 (page 19). We generally found that the shock pressure history recorded at F2 is relatively similar to that produced by the ESWL. We documented this in Fig. 50. On the other hand, there were a few differences that arose due to the differences in the

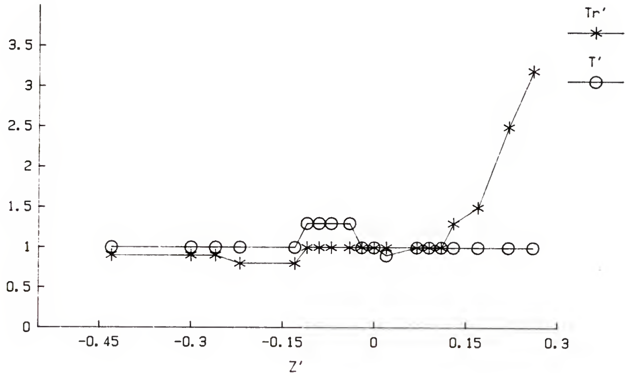

Fig. 49. Spatial distribution of the reflected shock duration and rise time along the reflector Z axis.

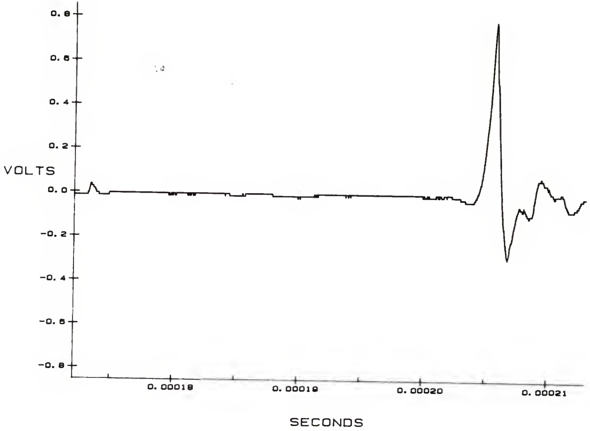

Fig. 50. EHL reflected shock pressure history produced at F2.

design of the reflector as well as the difference in the electrode spark gap size. In the EHL, the objective geometric second focus was found to be coincident with the dynamic focus. In other words, the objective geometric second focus carries the highest shock intensity. The pressure magnitude registered at F2 and produced by an available energy source of 5 joules (0.1 microfarad & 10 kV) measures about 81 atm. It should be noted here that the RSW pressure produced by an available energy of 400 joules (2 microFarad & 20 kV (3)) in the ESWL was 400 atm. We point out that the stainless steel reflector designed for the EHL experiment will reflect back more energy than that made of brass in the ESWL. This is due to the fact that the characteristic impedance of stainless steel is about 30 times that of the water, compared to about 20 times that of the water for the brass. This means that the energy reflected back is about 7% more than that in the case of using brass material.

The 9F electrode that we used with the EHL has advantages and disadvantages. That coaxial electrode wear rate is higher than that of a Dornier electrode. On the other hand, we observed that the performance of the electrode of the EHL in terms of the variations of the pressure magnitude from one shock to another is less. The coefficient of variation of the pressure produced by the EHL at F2 is estimated at 13%, compared to 22% by the ESWL. The reason behind this, we believe, is due to the electrode spark channel expansion rate. It is obvious from the design of the EHL electrode that there is more constraint at the poles of the expansion than in the case of the electrode in the ESWL. Furthermore, we found that the electrode spark gap of the EHL is much less than that of ESWL. Consequently, the energy density produced in the water by the electrode of the EHL is not very much less than that produced by the ESWL. It should be pointed out that the adjustment of the source of energy at F1 is very critical. A movement of as little as one millimeter can affect the focusing quality, the spatial distribution of the pressure, as well as the shock intensity at the objective focus (F2).

It can clearly be seen in Fig. 51 that the highest energy flux density and impulse of the RSW occurred at F2. Above F2, the decay of the RSW seems to be at a much faster rate than the buildup rate of either the impulse or the energy flux density.

The shock propagation velocity was barely above the sonic of about 1577 m/sec at the focus and it increases linearly in space along the direction of propagation even past F2. However, the Mach number never passed 1.1, as shown in Fig. 52.

We also observed a white light, accompanied by sound at F2, when the shock met with the transducer front surface. We think that such a sonoluminencence is due to a cavitation collapse.

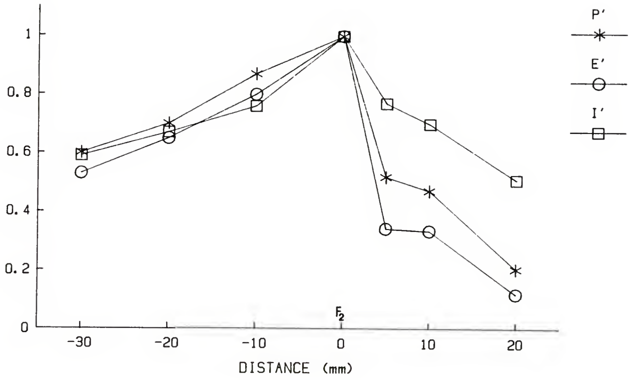

Fig. 51. Spatial distribution of EHL reflected shock pressure, impulse and energy flux density along the reflector Z axis measured from F_2.

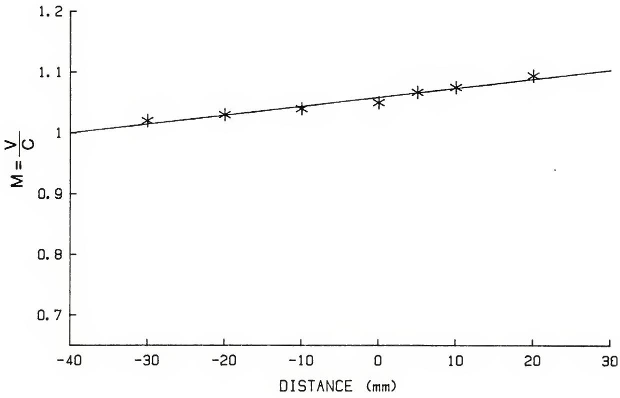

Fig. 52. Spatial distribution of the propagation velocity of the reflected shock, produced by EHL, normalized to the sonic velocity of the water along the Z axis of the reflector.

Cavitation Phenomenon at the First Focus (F1)

Numerous problems arose in measuring the relatively small magnitude of the long delayed secondary shock resulting from the collapse of the cavitation bubble formed at F1. In addition, there were numerous technical difficulties encountered when attempting to record the cavitation phenomenon on film using a high speed movie camera. Despite such difficulties, a fairly satisfactory description of the temporal behavior of the cavitation bubble at F1 has been reached.

The series of frames shown in Fig. 53 records the cavitation bubble life history. The time interval between these frames is nearly equal. It is evident that the bubble is of spherical shape and its life time is about 2.7 milliseconds before collapse. The bubble life time involves four stages: 1) the bubble formation and expansion phase, 2) the equilibrium state, 3) the fully developed stage and 4) the contraction phase and eventual collapse. In the stage labelled 1, the cavitation bubble is initiated about 0.45 milliseconds after the first appearance of the spark discharge. The bubble then starts and continues to expand outward at a gradually decreasing rate, as shown in Fig. 48. When the bubble reaches the equilibrium state, the expansion rate holds momentarily constant. At this stage, labelled 2, the bubble diameter (termed the equilibrium diameter) was measured to be 3.6 cm. The bubble then overexpands for a short time after the equilibrium state. During this time,

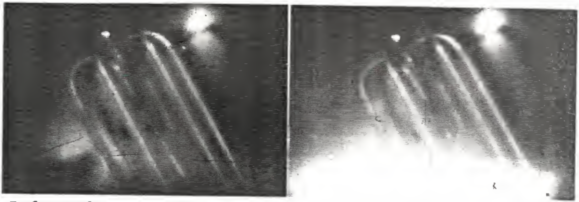

Before electrical discharge

The spark initiating light (t=0)

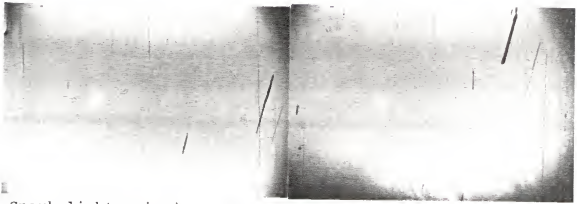

Spark light emission (150 microseconds)

(300 microseconds)

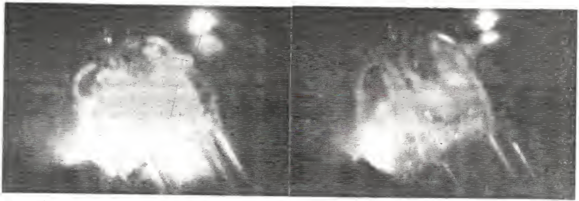

Cavitation bubble starts to (450 microseconds)

Bubble is expanding form (600 microseconds)

Fig. 53. Formation of cavitation bubble at F1.

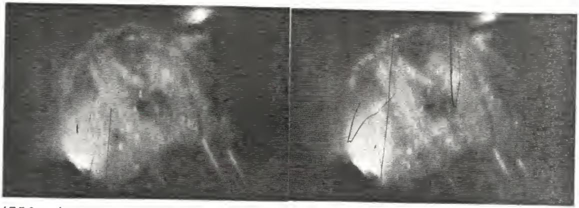

(750 microseconds) (900 microseconds)

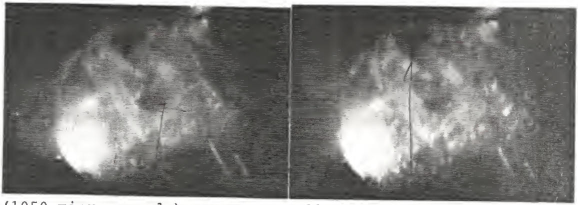

(1050 microseconds) Bubble reaches the equilibrium state (1200 microseconds)

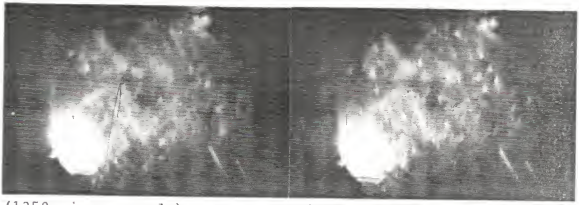

(1350 microseconds) Bubble continues to overexpand (1500 microseconds)

Fig. 53. Continued.

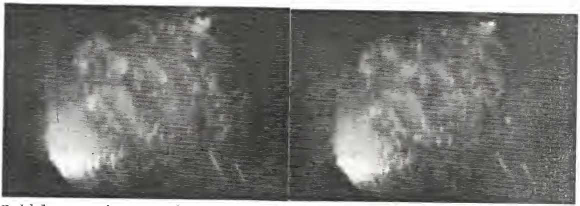

Bubble reaches maximum diameter (1650 microseconds)

Expansion stops and bubble maintains full size (1800 microseconds)

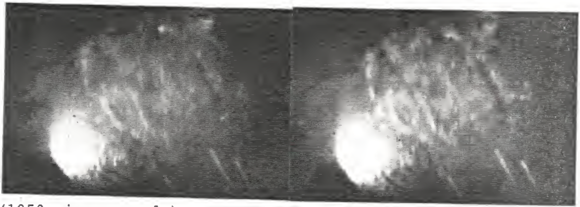

(1950 microseconds)

Bubble contraction phase starts (2100 microseconds)

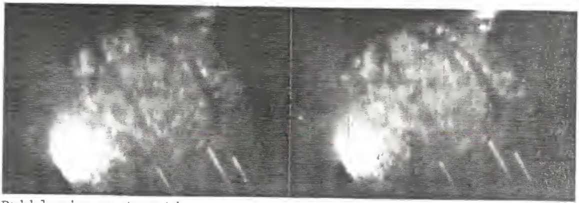

Bubble is contracting (2250 microseconds)

(2400 microseconds)

Figure 53. Continued.

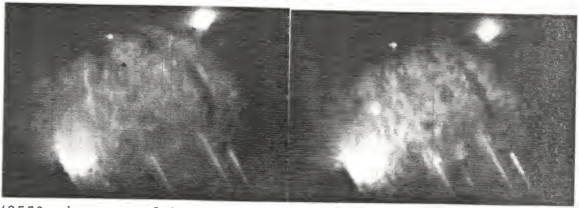

(2550 microseconds) (2700 microseconds)

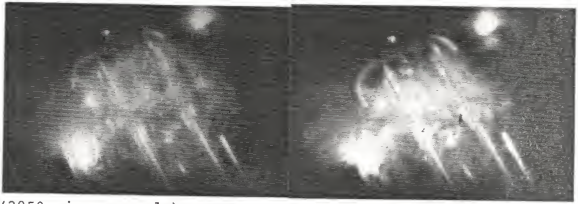

(2850 microseconds) (3000 microseconds)

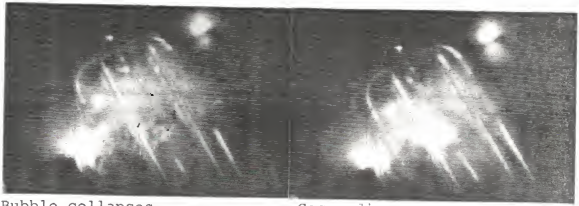

Bubble collapses
(3150 microseconds)

Gases disperse
((3300 microseconds)

Fig. 53. Continued.

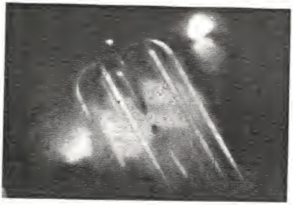

(3400 microseconds)

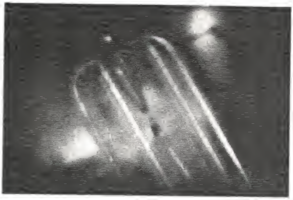

Gases continue to disperse.
(3550 microseconds)

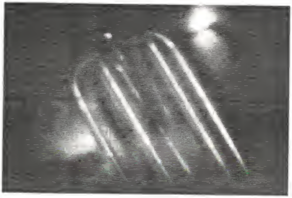

(3700 microseconds)

Fig. 53. Continued.

the pressure of the contained plasma falls below that of the surrounding hydrostatic pressure. The overexpansion is brought to a halt (about 1.2 milliseconds) after the first light emission from the spark. This is shown in Figs. 54 and 55. At this stage, labelled 3, the bubble reaches its maximum, fully developed, diameter of about 3.7 cm. During this stage, the bubble maintains its shape and size for about 0.3 milliseconds and $D' = D_i/D_m$ reaches a value of unity where D_m denotes the maximum bubble diameter and D_i is the bubble diameter at a certain frame number, i. The time between frames is 150 microseconds.

Physically, when the gas bubble overexpands, it has to be recompressed in order to satisfy the condition of continuity of the pressure at the bubble-water interface. The bubble thus starts stage 4, at about 2.1 milliseconds after spark initiation. It contracts at an increasingly rapid rate, as shown in Fig. 54. During this stage, the mean pressure of the contained plasma exceeds that of the surrounding water. When the bubble approaches the end of the contraction process, the bubble loses its sphericity and reaches its minimum diameter, which is about 2.74 cm, before final collapse.

In order to describe the history of the bubble rate of expansion and contraction, we need to define two terms: the bubble diameter increment or decrement normalized to the bubble maximum diameter, D', by the equation

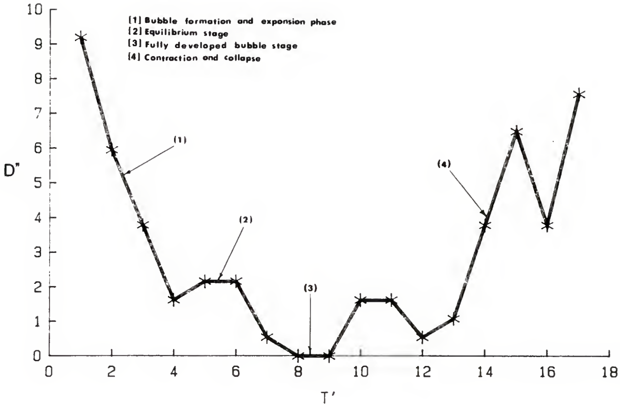

Fig. 54. Bubble expansion and contraction rate. T' is the time interval between frames normalized to the time of the beginning of the bubble formation and D" is the bubble diameter increment or decrement normalized to the bubble maximum diameter.

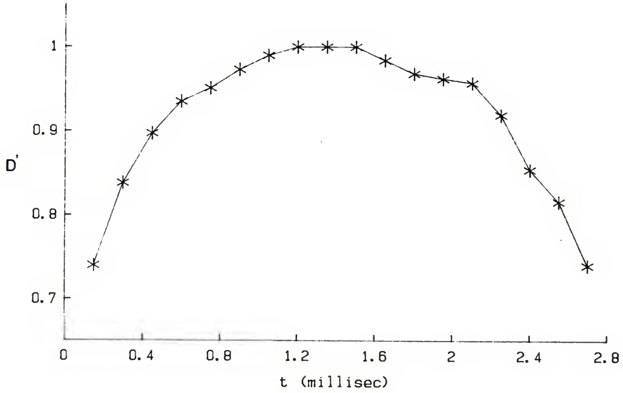

Fig. 55. Cavitation bubble diameter as a function of time where D' is the diameter normalized to the maximum diameter of the bubble.

$$D'' = 100\ (D'_{i+1} - D'_{i}) \qquad 2 < i < 19 \tag{33}$$

and T' is defined as the frame time interval normalized to the time of the beginning of the bubble formation, T_1, by

$$T' = (T_{i+1} - T_1)/T_1 \quad . \tag{34}$$

As a result of the expansion and contraction of the bubble, a considerable radial displacement of the water occurs but the changes in velocity take place at a much slower rate than in the initial phases of the motion immediately following explosion. Furthermore, throughout the expansion and contraction phases, the bubble remains stationary. In other words, the bubble neither migrates or pulsates. This finding is not in agreement with cavitation brought about by detonations where the bubble moves an appreciable distance upward and pulsates (i.e., the bubble reverses its motion from full contraction to expansion so abruptly as to be virtually discontinuous on a time scale suitable for the rest of the motion).

A further qualitative feature of significance is the fact that the bubble retains its sphericity (except near collapse) and remains fairly symmetrical despite the large radial accelerations, the appreciable contraction rate and the surrounding water motion.

It should be mentioned that the maximum velocity of the expansion of the bubble surface as it approaches its maximum radius is about 627 cm/sec, while the maximum velocity of the contraction of the bubble surface as it approaches its minimum radius is about 750 cm/sec. It is a common assumption that the changes in the density of the water surrounding the bubble are neglected. That assumption gets increasingly poor as the bubble approaches it minimum radius for which much larger pressures and accelerations are involved. At this radius, a secondary pressure wave or bubble pulse is emitted. It is to be expected that the description based on the assumption will be more successful in accounting for the general properties, such as the period, the velocity and the maximum radius, since there is negligible energy loss in that regard. On the other hand, that non-compressive theory is not adequate to describe the phenomena of the pressure wave emitted at collapse since the density and compressibility of the surrounding medium will undergo changes [42].

It is expected that the secondary shock wave emitted at the first focus will also decompose into a direct and a reflected shock component. The intensity of these SSWs is a function of the bubble size and its life time, factors that are directly dependent on the generating input voltage and the electrode spark gap size, as well as the depth at which the spark is fired. Only the reflected secondary pressure wave component reaches the second focus and has been detected as shown in Fig. 26. The direct secondary shock appears to dissipate during its propagation along the Z axis.

The energy dissipated as heat in the water between the electrode gap and the pressure gauge in the formation of the shock waves, radiation, heating of the gas, and dissociation in the channel is not readily measurable. Using equation (22) and given the collapse time which is 0.154 milliseconds, we calculated the mean pressure of the gas to be about 12.7 MPa. The energy stored in the gas bubble has been calculated by equation (21) to be about 338 joules. That estimate is based on noncompressive theory. It should be mentioned that Ramsauer [37], who made the earliest systematic measurements of the motion of gaseous explosion products, computed the energy available after emission of the shock wave at about 45% of the total energy. This, however, does not seem to apply in our case.

Furthermore, we have observed light emitted during and after the collapse of the bubble. This phenomena occurs due to the incandescence of the gas in the bubble resulting from the high pressures and temperatures during collapse. Physically, this sonoluminescence might be due to the recombination of the free ions produced by thermal dissociation of the molecules on the bubble surface [43].

Shock Test of Simulated Urinary Stones

Studying the effectiveness of both the focused shock wave and the cavitation-induced secondary shock at F2 as fracture mechanisms on materials, we first studied their effect on urinary concretion fragment size [6]. In this study, we used a standard material called "Z-brick." It was found that the percentage of the particle size which is smaller than 1 mm is highest away from the geometric focus (F2) at a distance along the Z axis of between 30 mm and 50 mm, as shown in Fig. 56. However, the fracture patterns were not examined at that time.

Recently, we have investigated the fracture patterns and the fracture mechanisms in simulated urinary test concretions. In the first stage of the experiments, we modelled the urinary stones in terms of their compressive strength using plaster cement and water. Watanabe [58] has divided the urinary stones into two categories: soft stones and hard stones. He found that the compressive strength of the soft type is about 65 atm, while that of the hard type is 180 atm. Based upon that, we found that samples made from 4 parts gypsum and 3 parts water and of length (L) to diameter (D) ratio equal 1 can acquire the compressive strength of the soft type of stone after leaving them to dry in air for 24 hours, while samples made of 3 parts gypsum and 1 part water and of the same dimension acquire a compression strength of about 180 atm after drying in air for 6 hours.

Changing the D/L ratio to 2, we found that those samples made of 2 parts gypsum to 1 part water reach 180 atm compression strength, after drying in air for 24 hours. On

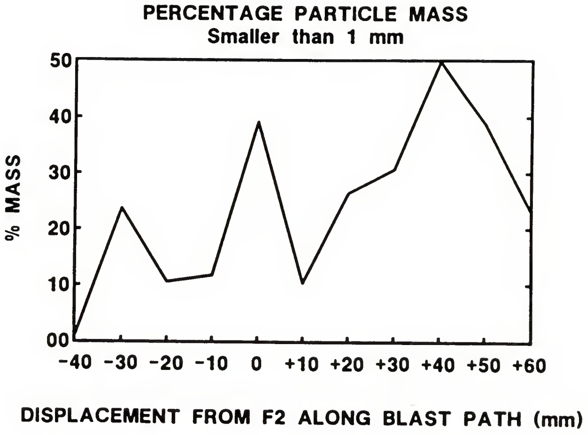

Fig. 56. Fracture of simulated urinary concretion (Z brick) along the Z axis.

the other hand, samples of the same dimension made of 1 part gypsum to 1 part water reach 65 atm, after leaving them to dry in air for 12 hours. The correlation between the amount of water and the weight of gypsum with time is shown in Fig. 25. The simulated urinary test concretions were used in a shock fracture test with the ESWL. The experiment was performed by holding the samples in a rigid clamp keeping them fully submerged under the water. It should be pointed out that the samples' lateral sides were constrained from deformation by constraints. This allowed us to limit our analysis to uniaxial strain, which is along the direction of the shock propagation. The samples were placed in the clamp in such a way that the frontal surface area, which is about to receive the incident shock wave, is perpendicular to the shock wave propagation direction, which is 14.28 degrees to the horizontal level in the ESWL.

The experiment was run at a temperature of 37C with a constant input voltage of 20kV and a rather new electrode (200 shots). In addition, the X-ray coupling balloons were kept deflated.

The first set of samples were tested at F2 and examined after a different number of shocks had impinged. The results are summarized in Fig. 57. It is found that after 10 shots, the front surface of the sample (compressive strength of 180 atm) which is receiving the shock appears to be roughened more than the back face, however, nothing major happened on either face of the sample. At 15 shots the

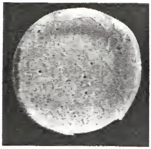

Front face after
10 shots.

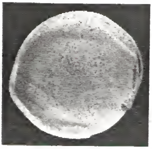

Back face after
10 shots.

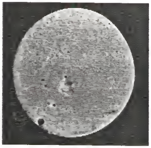

Front face after
15 shots.

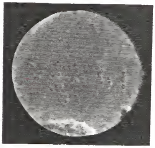

Back face after
15 shots.

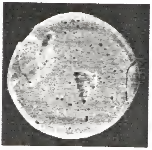

Front face after
20 shots.

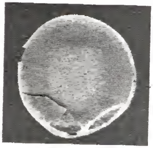

Back face after
20 shots.

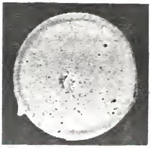

Front face after
30 shots.

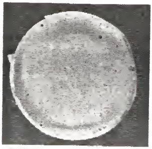

Back face after
30 shots.

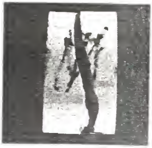

Sample side after
30 shots.

Fig. 57. Fracture patterns of shock tested concretions.

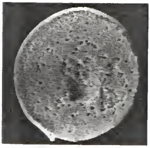

Front face after 40 shots.

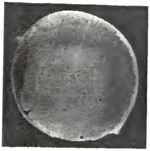

Back face after 40 shots.

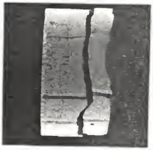

Sample side after 40 shots.

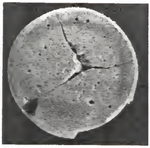

Front face after 55 shots.

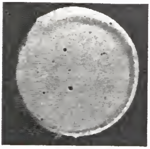

Back face after 55 shots.

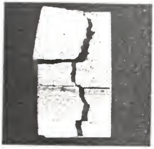

Sample side after 55 shots.

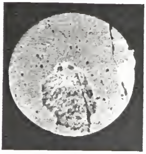

Front face after 40 shots at Fd.

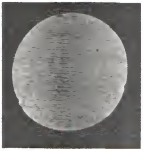

Back face after 40 shots at Fd.

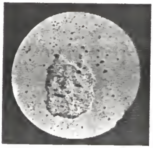

Front face after 40 shots 10 mm above F2.

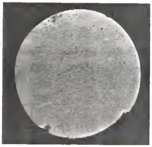

Back face after 40 shots 10 mm above F2.

Fig. 57. Continued.

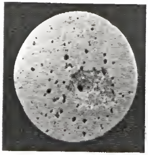

Front face after
40 shots 20 mm
above F2.

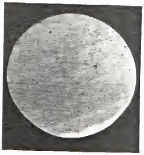

Back face after
40 shots 20 mm
above F2.

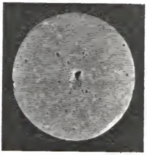

Front face after
40 shots 25 mm
above F2.

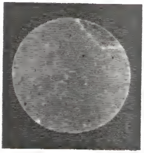

Back face after
40 shots 25 mm
above F2.

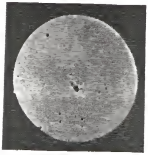

Front face after
40 shots 30 mm
above F2.

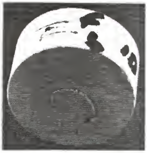

Back face after
40 shots 30 mm
above F2.

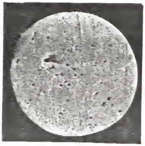

Front face after
40 shots 40 mm
above F2.

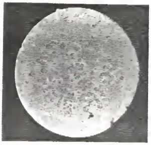

Back face after
40 shots 40 mm
above F2.

Fig. 57. Continued.

front face seemed to acquire a small dent while the back side registered a chipping off its edge. At 20 shots the dent on the front side became larger in area but the depth was maintained almost the same. A big chip, on the other hand, came off the front while the back face seemed to have suffered a tensile stress on reflection of the transmitted wave. The crack first started at about 2 mm away from the back face and toward the front surface. The crack propagated in a rather rough way through the material, and then stopped after splitting off a little fragment. At 30 shots, the front side appeared to have a small dent about the size of the previous sample. The back side did not seem to acquire any damage. On the other hand, at about 2 mm from the back side, there again appeared to be a big crack which propagated through the entire sample area dividing the sample into two separate disks. This fracture was definitely due to the tensile stress generated on reflection off the free back face. At 40 shots, there seemed to be the same crack described above. In addition, the back face was broken into two pieces, as well as a chipping off the front surface; however, this was not deep. At 55 shots, the same fracture occurred almost through the entire sample and it seemed to stop on breaking the front face into three pieces. The back face did not suffer any damage at all.

The second set of samples, which were made of the same materials and the same proportion (Fig. 57), were examined along the Z axis at different standoff distances of 5 mm, 10 mm, 20 mm, 25 mm, 30 mm, and 40 mm away from F2. Every sample received the same number of 40 shots. At 5 mm (at Fd) the front surface suffered a surface chipping besides a damage to the edge. The back face however, did not seem to have any sign of damage at all. At 10 mm there seemed to be the same surface chipping off the front face; however, it became smaller in area and less in depth than that at 5 mm. The back side did not suffer even a scratch. At 20 mm, the chipping off the front surface was much smaller and showed no sign of damage on the back face. At 25 mm, the back side edge suffered a fracture which seemed to be caused by tensile stress, while the front side registered a much smaller dent. At 30 mm, a very small dent registered on the front face, while the back face of the cylindrical sample appeared to suffer a tensile stress with the pulling of a piece out of it. At 40 mm, the dent on the front surface became less deep, while the back surface seemed to be roughened.

It is clear that the chipping action is due to the cavitation formed at F2. The fracture is definitely the largest at F2 even though we found previously that the highest shock intensity was 5 mm away from F2. Actually, there is no contradiction. The reason is that due to the concrete impedance, which is much higher than that of water, the reflected shock wave becomes focused at a finite distance away from Fd.

It is known that urinary concretions are more susceptible to fracture by tensile stress than by compressive stress. Hence, the tensile stress is the major mechanism for the breaking of kidney stones. However, there must exist an additional requirement for the shock wave to be effective as a fracture mechanism. This requirement is that the shock wave duration must be shorter than the transit time through the stone to help avoid any superposition of the entering and the reflected shock's components, an event that may reduce or even destroy the developed tensile stress.

CHAPTER V

SUMMARY AND CONCLUSIONS

The underwater explosion phenomenon generated by a short duration electrical discharge at the first focus of a semi-ellipsoidal reflector in the ESWL has been shown to be a complex phenomenon. It leads to more than one shock wave. These shock waves are the DSW, the RSW and the SSWs produced by the collapse of cavitation bubbles, formed at F1 and F2 of the reflector.

Our objective in this investigation has been to study such shock waves within a lithotriptor in terms of their evolution, propagation and focusing as well as their effect on materials.

The generation of the shock waves in water was found to be due to dielectric breakdown and vaporization. That finding was based on the level of the energy density within the spark channel.

We have studied the individual characteristics and contributions of the shock waves in water medium by fast response pressure transducers as well as a high speed movie camera. The pressure history of the explosion generated has been recorded as a function of time starting at t=0 which marks the time of the voltage discharge at the first focus F1. About 150 microsec later the shock wave (DSW) has reached F2 directly from F1 by propagation along the Z axis. The reflected and focused shock wave (RSW) registers at F2 30 microsec after the arrival of the direct shock. At 830 microsec after the initial discharge there appeared a third shock wave attributed to the cavitation bubble collapse at F2. About 1.2 millisec after discharge the reflected component of the secondary shock wave produced by the collapse of the cavitation bubble at F1 reaches F2. The direct component is not observed at F2 and thus must have fully dissipated during direct propagation from F1 and F2.

The shock waves generated in water can be affected by the geometry and properties of the reflector in the generating machine (ESWL). These characteristics have been studied in terms of the effect of the electrode spark separation, the inflation of the para-ellipsoid X-ray balloons, the input voltage and the carrier water condition on the intensity and the focusing quality of the RSW. We found that the rate at which the electrode spark gap wears out (i.e. gap spacing widens) is a logarithmic function of the number of discharges. The electrode spark gap size has proven to be a factor which can influence the shock pressure field. In other words, the drop off in pressure amplitude for increasing distance from the objective focal point F2 is found to depend on the electrode spark separation. The large gap electrodes of 2.8 mm spacing yield optimum pressure fields with almost uniform shock intensity.

In investigating the effect of the inflation of the X-ray coupling balloons we did not find a large decrease in the pressure magnitude when the balloons are inflated (but not overlapped on the reflector). Furthermore, the effect of the discharge voltage on the RSW was as has been expected. We found that higher input voltage gave higher shock wave pressure, impulse and energy flux, density, shorter shock duration and faster rise time.

It is also found that the longer the exposure of the degassed water to the environment, the lower the pressure magnitude of the RSW at F2. It should be mentioned that the temperature of the water has no effect on the shock waves generated directly by the electrical discharge; however, it might have an effect on the secondary pressure waves generated by the collapse of cavitation bubbles.

By analyzing the direct shock pressure along its direction of propagation, it is found that at the second focus (F2) the pressure rise time is about 400 nsec and the fall time is about 600 nsec based on 10% to 90% of each duration. The total shock duration, based on 50% of the pulse width, was about 800 nsec. The pressure amplitude found was about 12 atm and the energy flux density reached 0.6 Pa•m, while the impulse was 1 Pa•sec.

The direct shock wave has been described at F2 in the time domain to have an approximately linear rise to its maximum amplitude as well as a linear decay to the ambient condition. The pressure as well as the shock impulse of the DSW has proven to satisfy the 1/R law which is based on explosive generated spherical shocks. The energy flux density decays according to a power law. The shock rise time and its duration have been correlated to one another and we found that the faster the shock rise time the shorter its duration.

Investigating the contribution of parts of the shock wave region to both the impulse and the energy flux density at F2, we found that the energy transported by the shock through a fixed surface area increases with time over its duration. In other words, it is not only the shock front which contributes to the shock intensity. By examining the shock front movement, it was found that the propagation velocity is about 1667 m/sec or 1.1 times the speed of sound in water. The shock front propagates with a fixed velocity along its path. Given the pressure jump at the second focus, the density behind the shock front is found to be about 1000.5 kg/m. It is obvious that the density change is very small. The compressibility coefficient is estimated to be about 1.0005. Also the particle velocity behind the shock front was estimated to be about 1 m/sec based on calculations. In addition, the shock front thickness is estimated to be 670 microns based on the average rise time of 400 nsec.

After the arrival of the DSW, the RSW reaches F2 30 microseconds later. Analyzing the properties of the RSW in the time domain, we found that it is not necessarily true that the geometric focal point will be the location of the highest pressure. In fact the highest pressure magnitude was found at 5 mm beyond the geometric focus (at JHMHC). This position along the Z axis is termed the dynamic focus (Fd). The position of the dynamic focus has been shown to differ from one ESWL to another and it should be pointed out that the pressure increase at the dynamic focus is only about 5% above that at the geometric focus.

The RSW pressure rises linearly in time to its maximum magnitude of 400 atm at Fd in about 450 nsec. Similarly the pressure magnitude falls off linearly in time to the ambient condition within about 575 nsec based on the 10-90% rule. The duration of the entire shock wave is 550 nsec at Fd based on half width rule.

The shock impulse, that is, the momentum imparted to the water by the shock front passage and the energy flux density behind the shock front have been measured at Fd to be 28.4 Pa•sec and 115 Pa•m, respectively. The buildup of the impulse and the energy flux density increases dramatically over the shock duration.

The shock propagation velocity is found to increase with distance along the shock propagation direction. It was clearly seen that the RSW propagates supersonically at about Mach 1.18 at Fd. It is believed that the increase of the shock front velocity for increasing distance is a result of the superposition of the shock waves along the propagation direction. In other words, it is due to the convergence and coherence of the shock waves along the propagation direction. The shock propagation velocity at the second focus is about 1770 m/sec.

The shock front thickness at Fd as well as the dynamic viscosity have been estimated to be 800 microns and 1453 Pa•sec respectively based on a rise time of 450 nsec. The compressibility coefficient, however, has reached about 1.018, based on the assumption that the inertial forces are in equilibrium with the viscous forces. The density behind the shock front was estimated to be about 1018 kg/m. From the conditions ahead of the shock front, the particle velocity behind the shock front has been calculated to be 23.4 m/sec.

Some variation in the pressure magnitude was noticed from one shock to the next. It is most likely that variation of the velocity of the electrode spark channel expansion causes this variation, over which there is little control.

In analyzing the reflected shock wave in the frequency domain, it was found that the maximum power of the shock occurs at almost zero frequency level. This finding explains why the ESW is an effective fracture mechanism particularly since high frequency signals are strongly attenuated in liquids.

The spatial distribution of the RSW intensity has been studied along the Z axis. We found that the pressure rises to its maximum value almost exponentially. The decay of the pressure in space along the Z axis, can be divided into three parts. In the first stage the pressure drops sharply. It is believed that once past the dynamic focus the field diverges and consequently the pressure falls off. In addition, an expanding wave forms and consequently a tensile stress starts to be generated. Tensile stress waves in water when superimposed over the compressive stress will result in lowering of the magnitude of the compressive stress drastically. The second part of the pressure spatial distribution is that the pressure rises in magnitude again. It seems that at this point the tensile effect starts to fade out until it becomes negligible. During the third part the pressure is back on its exponentially decaying pattern. It was also evident that the energy flux density stored behind the shock front rises more rapidly than does the pressure. The highest magnitude of the shock impulse is clearly in the focal region.

In examining the dissipation of the focused shock with respect to the direct shock along the propagation direction, it was found that the reflected shock pressure decays in space exponentially. From the distribution of the shock wave duration and its rise time along the Z axis, it is clear that the duration is shortest at the dynamic focal point while the rise time seems to be about the same order of magnitude, around the second focus, of about 450 nsec.

Cavitation generally follows the evolution of the shock waves. Specifically speaking, cavitation bubbles appear twice; once at the first focus (F1) and then again at the second focal region of the reflector. The former is due to superheating of the water, as a result of the high temperature generated from the spark, while the latter is due to such a drop in the water pressure after the shock wave passes that the vapor pressure is reached.

It was clearly shown that the pressure magnitude of the secondary shock wave produced by collapse of the cavitation bubble recorded at F2, shown in Fig. 58, is about 20% of the magnitude of the focused shock. The formation of the second cavitation bubble occurs at Fd where the highest pressure is observed.

Using a high speed movie camera to record the cavitation bubble at F1, we found that the bubble is of spherical shape and its life time is about 2.7 milliseconds. The life time involves four stages; the first stage begins when the cavitation bubble forms and then starts to expand outward at a gradually decreasing rate of expansion through an equilibrium state where the expansion rate holds momentarily. The bubble then overexpands until the mean pressure inside it

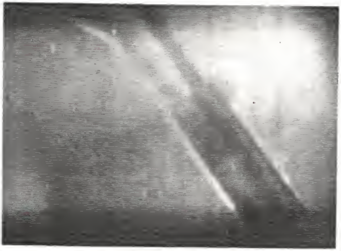

Electrical discharge t=0.

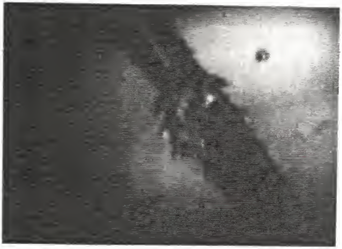

Bubble formation t=150 microsec.

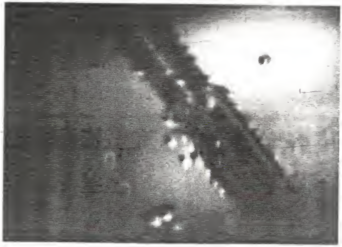

Bubble expansion 300 microsec.

Fig. 58. Cavitation bubble formation at F2.

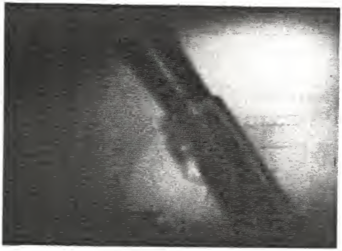

Bubble contraction t=450 microsec.

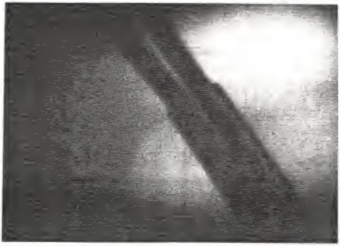

Bubble collapse t=600 microsec.

Fig. 58. Continued.

falls below the pressure in the compressed water surrounding it. At this stage the bubble reaches its maximum diameter of about 3.7 cm, and it becomes fully developed. The expansion is then brought to a rest where the bubble momentarily maintains its shape and size. The bubble next starts its third stage where it contracts at an increasingly rapid rate until its mean pressure exceeds that in the surrounding water. During the contraction process the bubble loses its sphericity and reaches its minimum diameter at about 2.74 cm before it collapses. Furthermore, throughout the expansion and contraction phase of the bubble, the bubble center remains fixed.

A further qualitative feature of significance is the fact that the bubble retains its sphericity (except near collapse) and remains fairly symmetrical despite the large radial accelerations, the appreciable contraction rate and the surrounding water motion.

The maximum velocity of the bubble surface as it approaches its maximum radius is about 627 cm/sec, while the maximum velocity of the bubble surface as it approaches its minimum radius is about 750 cm/sec. The bubble life time and the time scales will of course change with the electrode gap width and the discharge voltage.

It is found that the mean pressure of the gas within the cavitation bubble is about 12.7 MPa. The energy stored in the gas bubble has been calculated to be about

338 joules. That estimate is based on the noncompressive theory [67].

Furthermore, we have observed that light is emitted during and after bubble collapse. That phenomenon occurs due to the incandescence of the gas produced by the high pressures and temperatures during collapse. Physically this sonoluminescence is believed to be due to the recombination of the free ions produced by thermal or mechanical dissociation of the molecules on the bubble surface [61].In examining the effect of shocks on the fracture patterns of simulated urinary concretions, modelled to match the compressive strength of the urinary calculi, we found that there are more than one fracture mechanism near the focal region (F2). Compression effects are observed at the focal region. This compression is due to the converging shock wave in addition to the secondary shock wave emitted by the collapse of the bubble at F2. The compressive stress produces tensile stress upon reflection at the specimens free back face, causing spalling. It should be mentioned here that the spalling has to be preceded by fatigue in order for the specimens to fracture. About 30 mm beyond the focal region we found a different fracture pattern due to tension effects. It should be pointed out that in these studies the samples' sides were constrained. This will allow only unidirectional (the direction of the shock propagation) strain field to be considered. It was clear that the observed chipping action is due to the cavitation formed at F2. The fracture is definitely the largest at F2. That finding does not contradict our observation that the highest pressure occurs at 5 mm beyond F2, i.e. at Fd. The reason for this agreement is that due to higher impedance of concrete the reflector shock wave becomes focused at a distance below Fd.

It is known that concretions are more susceptible to fracture produced by tensile stress than by compressive stress and thus tensile stress is also the major mechanism for the breakup of urinary calculi. One way to produce a higher tensile stress was found by triggering two consecutive shock waves. As shown in Fig. 59, the superposition of two focused shocks produces a tensile stress whose amplitude is about 50% higher than that produced by a single shock wave. This finding deserves further investigation. One requirement, which should be considered though, for the shock wave to be effective as a fracture mechanism, is that the shock wave duration must be shorter than the transit time through the stone to help avoid any superposition of the entering and the reflected shocks components.

We also think that the effect of two focused shocks sharing the same objective focus and triggered simultaneously so that they propagate toward each other and eventually collide head-on at the focus will optimize the fracture mechanism of urinary calculi.

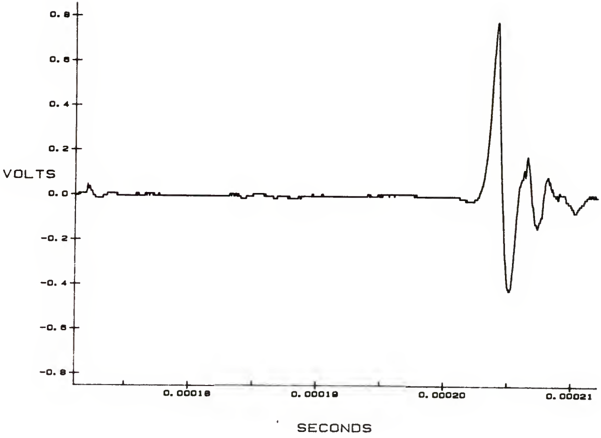

Fig. 59. Two superimposed reflected shocks generated by the EHL.

REFERENCES

1. Mitchell, M.E., and Kerr, W.S., Jr., "Experience with the Electrohydraulic Disintegratior," J. of Urol., Vol. 117, pp. 159-160, 1977.

2. Angeloff, A., "Hydroelectrolithtripsy," J. of Urol., Vol. 108, pp. 867-871, 1972.

3. Chaussy, C., Schmiedt, E. Jocham, D., Walther, V., and Brendel, W., "Extracorporeal Shock Wave Lithotripsy: New aspects in the treatment of kidney stone disease," Karger, Munich, West Germany, 1982.

4. Nasr, M.E., Studies on the fracture mechanism of urinary test concretions by lithotriptor devices, Master of Science Thesis, University of Florida, Gainesville, 1982.

5. Hunter, P.T., Finlayson, B., Hirko, R., Voreck, R., Walker, R., Walck, S., and Nasr, M., "Measurement of Shock Wave pressures used for Lithotripsy," J. of Urol., vol. 136, pp. 733-738, 1986.

6. Madorsky, M., Finlayson, B., and Nasr, M., "ESWL Blast Path Considerations Relevant to Patient Treatment Strategies," sent for publication in J. of Urol. 1986.

7. Early, H.C., and Martin, E.A., "The underwater spark; A photographic light source of high intrinsic brilliance", Elect. Engrs. I, vol. 74, pp. 788-790, 1955.

8. Rust, H.H., Drubba, H., "Practical application of the underwater spark as a source for echo sounding", Z. Angew. Phys. 5, 251, 1953.

9. Zingerman, A.S., "The dependence of the pressure at the front of a shock wave upon the steepness of the energy-pulse front when an electrical discharge takes place in liquid", Soviet Physics, Technical Physics, Vol. 1, pp. 2454, 1956.

10. Komel'kov, V.S., "Dielectric breakdown of liquids", Doklady Akad. Nauk SSSR vol. 47, pp. 269-272, 1945.

11. Skvortsov, Yu. V., Komel'kov, V.S., and Kuznetsov, N.M., "Expansion of a spark channel in a liquid", The Zhurnal Tekhnicheskoi Fiziki, Vol. 30, No. 10, pp. 1165-1177, 1960.

12. Martin, E.A., "Experimental Investigation of a high energy density, high pressure arc plasma," J. Appl. Phys., Vol. 31, pp. 255, 1960

13. Whitham, G.B., "A new approach to the problems of shock dynamics," part 1. Two-dimensional problems, J. Fluid Mech., vol. 2, pp. 146-171, 1957.

14. Whitham, G.B., "A new approach to the problems of shock dynamics," part 2. Three-dimensional problems, J. Fluid Mech., vol. 5, pp. 369-386, 1959.

15. Sturtevant, B., and Kulkarny, V.A., "The focusing of weak shock waves," J. Fluid Mech., vol. 73, pp. 651-671, 1976.

16. Hayes, W.D., "Similarity rules for nonlinear acoustic propagation through a caustic," second Cof. Sonic Boom Res., N.A.S.A. Special Publ. No. 180, pp. 165-171, 1968.

17. Pechuzal, G., and Kevorkian, J., "Supersonic-transonic flow generated by a thin airfoil in a stratified atmosphere," SIAM J. Appl. Math., vol. 33, pp. 8-33, 1977.

18. Cramer, M.S., and Seebass, A.R., "Focusing of weak shock waves at an arete," J. Fluid Mech., vol. 88, pp. 209-222, 1978.

19. Ting, T.C.T., and Herrmann, G., "Propagation of a shock wave front through a lens-shaped elastic body," J. Appl. Mech., vol. 41, pp. 691-696, 1974.

20. Cramer, M.S., "The focusing of weak shock waves at an axisymmetric arete," J. Fluid Mech., Vol. 110, pp. 249-253, 1980.

21. Gomes, S.J.F., and Al-Hassani, S.T.S., "Internal fractures in spheres due to stress wave focusing", Int. J. Solids and Struct., Vol. 13, pp. 1007, 1977.

22. Gomes, S.J.F., Al-Hassani, S.T.S., and Johnson, W., "Anote of times to fracture in solid perspex spheres due to point explosive loading", Int. J. Mech. Sci., Vol. 18, pp. 543, 1976.

23. Lovell, E., Al-Hassani, S.T.S., and Johnson, W., "Fracture in solid spheres and circular disks due to a point explosive impulse on the surface",Int. J. Mech. Sci., Vol. 16, pp. 193, 1974.

24. Chaussy, C., Schmiedt, E., Jocham, D., Brendel, W., Frossmann, B., and Walther, V., "First Clinical Experiences with Extracorporally Induced Destruction of Kidney Stones by Shock Waves," J. Urol., vol. 127, pp. 417-420, 1982.

25. Chaussy, C., Schmidt., E. Jocham, D., Schuller, J., Brendel, H., and Liedl, B. "Extracorporeal shock wave Lithotripsy for treatment of Urolithiasis," J. of Urol., Vol. XXII, No. 5, pp. 59-66, 1984.

26. Al-Hassani, S.T.S., and Gomes, S.J.F., "Internal fractures in paraboloids of revolution due to stress wave focusing," Inst. Phys. Conf. Ser., No. 47:Ch. 2, 1979.

27. Harrison, M., "An Experimental Study of Single Bubble Cavitation Noise," J. of Acoust. Soc. of Amer., Vol. 24, pp. 776-782, 1952.

28. Mellen, R.H., "An Experimental Study of the Collapse of a Spherical Cavity in Water, "J. of Acoust. Soc. of Amer., Vol. 28, pp. 447-457, 1956.

29. Shutler, N.D., and Mesler, R.B., "A Photographic Study of the Dynamics and Damage Capabilities of Bubbles Collapsing Near Solid Boundary," ASME J. of Basic Engineering, Vol. 87, No. 3, pp. 511, 1965.

30. Brunton, J.H., Wilson, M.P.W., and Camus, J.J., "The High Speed Photography of Liquid Flow in Collapsing Cavities and Impinging Liquid Drops," Proceeding of the 8th International Congress on High Speed Photography, Stockholm, pp. 467-470, 1968.

31. Kling, C.L., and Hommitt, F.G., "A Photographic Study of Spark-Induced Cavitation Bubble Collapse," ASME J. of Basic Engineering, Vol. 94, No. 4, pp. 825-833, 1972.

32. Fujikawa, S., and Akamatsu, T., "Experimental Investigations of Cavitation Bubble Collapse by a Water Shock Tube," Bulletin of the JSME, Vol. 152, pp. 223-230, 1978.

33. Fujikawa, S., and Akamatsu, T.Z., "Effects of the Non-Equilibrium Condensation of Vapour on the Pressure Wave Produced by the Collapse of a Bubble in a Liquid," J. of Fluid Mechanics, Vol. 97, Part 3, pp. 481-512, 1980.

34. Rayleigh, Lord., "On the Pressure Developed in a Liquid During the Collapse of a Spherical Cavity," Philosophical Magazine, Vol. 34, pp. 94-98, 1917.

35. Trilling, L., "The Collapse and Rebound of a Gas Bubble," J. of Applied Physics, Vol. 23, No. 1, pp. 14-17,1952.

36. Shima, A., Takayama, K., Tomita, Y., and Miura, N., "An Experimental Study on Effects of a Solid Wall on the Motion of Bubble and Shock Waves in Bubble Collapse," Acustica, Vol. 48, No. 5, pp. 293-301, 1981.

37. Ramsauer, C., "Die massenbewegung des wessers bei unter wasser explosionen", Ann. d. Phys. ser. 4, vol. 72, pp. 265, 1923.

38. Herring, C., "Theory of the Pulsations of the Gas Bubble Produced by an Underwater Explosion," NDRC Division 6 Report C4-sr20 (1941).

39. Jarman, P. "Measurements of sonoluminescence from pure liquids and some aqueous solution. "Proc. Phys. Soc., vol. 73, pp. 628, 1959.

40. Wheeler, W.H. "Indentation of metals by cavitation." ASME Trans., Series D, vol. 82 N1, pp. 184-194, 1960.

41. Hammitt, F.G., Cavitation and Multiphase Flow Phenomena, McGraw-Hill, New Jersey, 1980.

42. Harvey, E.N., Mcelroy, W.D., and Whiteley, A.H., "On cavity formation in water," J. Appl. Phys., vol. 18, pp. 162-172, 1947.

43. Pearsall, I.S., Cavitation, Mills & Boon Limited, 1972.

44. Frederick, J.R., Ultrasonic Engineering, John Wiley & Sons, Inc., 1965.

45. Neubert, K.H., Instrument Transducers: An introduction to their performance and design, Clarendon Press, 1975.

46. Warner, A.W., Onoe, M., and Coquin, G.A., "Determination of electric and Piezoelectric constants for crystals in class 3m," J. Acoust. Soc. Am., vol. 42, pp. 1223-1231, 1966.

47. Bottom, E.V., Introduction to quartz crystal unit design, Van Nostrand Reinhold Co., New York, 1982.

48. Herbert, J.M., Ferroelectric Transducers and Sensors, Gordon and Breach Science Publishers, New York, 1982.

49. Graham, R.A., "Lithium niobate stress transducers," SAND78-1911, Dec. 1978.

50. Graham, R.A., and Jacobson, R.D., "Lithium niobate stress gauge for pulsed radiation deposition studies," Appl. Phys. Lett., Vol. 23, No. 11, pp. 584, 1973.

51. Smith, R.T., and Welsh, F.S., "Temperature dependence of the elastic, piezoelectric, and dielectric constants of Lithium Tantalate and Lithium Niobate," J. Appl. Phys., Vol. 42, No. 6, pp. 2219-2230, 1971.

52. Reed, R.P., "A System for Measurement of Free Field Stress Waves Using Lithium Niobate Piezoelectric Transducers," SAND78, pp. 2, 1978.

53. Sigrist, M.W., "Mechanisms of Acoustic Wave Generation By Lasers," proceedings of the international conference on laser, pp. 525, 1981.

54. Halpin, W.J., Jones, D.E., and Graham, R.A., "A submicrosecond technique for simultaneous observation of input and propagated impact stresses," Symposium on dynamic behavior of materials, pp. 208-218, 1968.

55. Graham, R.A., Neilson, F.W., and Benedick, W.B., "Piezoelectric Current from Shock Loaded Quartz; a Submicrosecond Stress Gauge," J. Appl. Phys., Vol. 36, No. 5, pp. 1965.

56. Murri, W.J., Curran, D.R., Petersen, C.F., and Crewdson, R.C., "Response of solids to shock waves,", Adv. high pressures Res., vol. 4, pp. 1-163, 1974.

57. Lawrence, R.J., and Davidson, L.W., "Analysis of nonlinear plane wave propagation in piezoelectric solids," Proceedings of the Symposium on Application on Computers Methods in Engineering, Vol. II, pp. 941, 1977.

58. Murata, H., Watanabe, T., Takahashi, K. Watanabe, and S. Oinuma, Jap. J. Urol., Vol. 68, pp. 249, 1977.

59. Johnson, W., "Impact Strength of Materials," London, 1972.

60. Emmony, D.C., Geerken, T., and Klein, H., Baltik; J. Acoust. Soc. Am., vol. 73(1), pp. 1983.

61. Barnes, P.A., "Studies of laser induced breakdown phenomena in liquid water", Ph.D. Thesis (Simon Fraser U., 1969).

62. Bunkin, F.V., Karlov, N.V., Komissarov, V.M., and Kuz'min, C.P., JETP Lett., vol. 13, pp. 341-343, 1971.

63. Botygina, N.N., Bukatyi, V.I., and Khmeievtsov, S.S., "Generation of sound waves by interaction of a laser-pulse with water", Sov. Phys. Acoust., vol. 22, pp. 368-371, 1976.

64. Cleary, S.F., and Hamrick, P.E., "Laser-induced transients in the mammalian eye", J. Acoust. Soc. Am., vol. 46, pp. 1037-1044, 1969.

65. Sigrist, M., and Kneubuhl, F., "Spherical Model on Thermoelastic Generation of Acoustic Waves," Vol. 29, pp. 353-357, 1978.

66. Sigrist, M., and Kneubuhl, F., "Laser-generated Stress Waves in Liquids," J. Acoust. Soc. Am., vol. 64, pp. 1652-1663, 1978.

67. Cole, R.H., "Underwaer Explosion," Princeton Univ. Press, 1948.

68. Holt, M., "Underwater Explosions," Ann. Rev. Fluid Mech., vol. 9, pp. 187-214, 1977.

69. Courant, R., and Friedrichs, K.O., Supersonic Flow and Shock Waves, Interscience Publishers, Inc., New York, 1948.

70. Zel'dovich, and Rsizer, Yu. P., "The Physics of Shock Wzves and High Temperature Hydrodynamic Phenomena," Fizmatgiz, pp. 68, 1963.

71. Sabnis, G.M., and White, R.N., "A. Gypsum Mortar for Small-Scale Models," ACI Journal, Nov. 1967.

72. Bell, C.E., and Landt, J.A., "Laser-induced high-pressure shock waves in water", Appl. Ohys. Lett. vol. 10, pp. 46, 1967.

73. Gallagher, J., Simple Dielectric Liquids, Clarendon Press. Oxford, 1975.

74. Herzfeld, K.F., and Litovitz, T.A., "Absorption and Dispersion of Ultrasonic Waves, Academic, New York, 1959.

BIOGRAPHICAL SKETCH

Mohamed El Sayed Nasr was born in Egypt on July 31, 1954. After he had graduated from high school in Cairo in June 1972, he entered the College of Engineering and Technology (formerly called Cairo Institute of Technology, CIT) at Helwan University in Helwan, Cairo. He graduated with a Bachelor of Mechanical Engineering degree in May 1977, ranked the eighth on his group which was composed of 300 students. After his graduation, he was appointed by the Department of Mechanical Engineering to work as an instructor, teaching at the undergraduate level.

He began studying for higher degrees in October 1978 at Cairo University, Mechanical Engineering Department, however by January 1980, he was nominated to complete his higher studies in the United States. In January 1981, he entered the Engineering Science Department at University of Florida as a graduate student. He completed his Masters degree in July 1982 in the Engineering Sciences field.

In October 1982 he was nominated to continue his studies toward the doctorate degree. He completed his Ph.D. September 4, 1986 in the Mechanics field.

I certify that I have read this study and that in my opinion it conforms to acceptable standards of scholarly presentation and is fully adequate, in scope and quality, as a dissertation for the degree of Doctor of Philosophy.

Ulrich H. Kurzweg

Ulrich H. Kurzweg, Chairman
Professor of Engineering Sciences

I certify that I have read this study and that in my opinion it conforms to acceptable standards of scholarly presentation and is fully adequate, in scope and quality, as a dissertation for the degree of Doctor of Philosophy.

Birdwell Finlayson, Co-chairman
Professor of Surgery

I certify that I have read this study and that in my opinion it conforms to acceptable standards of scholarly presentation and is fully adequate, in scope and quality, as a dissertation for the degree of Doctor of Philosophy.

Lawrence Malvern

Lawrence Malvern
Professor of Engineering Sciences

I certify that I have read this study and that in my opinion it conforms to acceptable standards of scholarly presentation and is fully adequate, in scope and quality, as a dissertation for the degree of Doctor of Philosophy.

Edward Walsh

Edward Walsh
Professor of Engineering Sciences

I certify that I have read this study and that in my opinion it conforms to acceptable standards of scholarly presentation and is fully adequate, in scope and quality, as a dissertation for the degree of Doctor of Philosophy.

Arun Kumar Varma

A. Varma
Professor of Mathematics

I certify that I have read this study and that in my opinion it conforms to acceptable standards of scholarly presentation and is fully adequate, in scope and quality, as a dissertation for the degree of Doctor of Philosophy.

Harold Doddington
Professor of Engineering Sciences

I certify that I have read this study and that in my opinion it conforms to acceptable standards of scholarly presentation and is fully adequate, in scope and quality, as a dissertation for the degree of Doctor of Philosophy.

Charles Taylor
Professor of Engineering Sciences

This dissertation was submitted to the Graduate Faculty of the College of Engineering and to the Graduate School and was accepted as partial fulfillment of the requirements for the degree of Doctor of Philosophy.

December 1986

Hubert A. Bevis
Dean, College of Engineering

Dean, Graduate School